



SIGNAL 2024

The Ninth International Conference on Advances in Signal, Image and Video
Processing

ISBN: 978-1-68558-142-8

March 10th –14th, 2024

Athens, Greece

SIGNAL 2024 Editors

Pavel Loskov, ZJU-UIUC, China

Atreyee Sinha, Edgewood College, USA

SIGNAL 2024

Foreword

The Nineteenth International Conference on Advances in Signal, Image and Video Processing (SIGNAL 2024), held between March 10 – 14, 2024, continued the inaugural event considering the challenges mentioned above. Having these motivations in mind, the goal of this conference was to bring together researchers and industry and form a forum for fruitful discussions, networking, and ideas.

Signal, video and image processing constitutes the basis of communications systems. With the proliferation of portable/implantable devices, embedded signal processing became widely used, despite that most of the common users are not aware of this issue. New signal, image and video processing algorithms and methods, in the context of a growing-wide range of domains (communications, medicine, finance, education, etc.) have been proposed, developed and deployed. Moreover, since the implementation platforms experience an exponential growth in terms of their performance, many signal processing techniques are reconsidered and adapted in the framework of new applications. Having these motivations in mind, the goal of this conference was to bring together researchers and industry and form a forum for fruitful discussions, networking, and ideas.

We take here the opportunity to warmly thank all the members of the SIGNAL 2024 Technical Program Committee, as well as the numerous reviewers. The creation of such a high quality conference program would not have been possible without their involvement. We also kindly thank all the authors who dedicated much of their time and efforts to contribute to SIGNAL 2024. We truly believe that, thanks to all these efforts, the final conference program consisted of top quality contributions.

Also, this event could not have been a reality without the support of many individuals, organizations, and sponsors. We are grateful to the members of the SIGNAL 2024 organizing committee for their help in handling the logistics and for their work to make this professional meeting a success.

We hope that SIGNAL 2024 was a successful international forum for the exchange of ideas and results between academia and industry and for the promotion of progress in the field of signal processing.

We are convinced that the participants found the event useful and communications very open. We also hope that Athens provided a pleasant environment during the conference and everyone saved some time for exploring this beautiful city

SIGNAL 2024 Chairs:

SIGNAL 2023 Steering Committee

Wilfried Uhring, Université de Strasbourg, France

Jérôme Gilles, San Diego State University, USA

Constantin Paleologu, Polytechnic University of Bucharest, Romania

Sergey Y. Yurish, Excelera, S. L. | IFSA, Spain

Pavel Loskot, ZJU-UIUC Institute, China

SIGNAL 2024 Publicity Chairs

Sandra Viciano Tudela, Universitat Politècnica de Valencia, Spain

José Miguel Jiménez, Universitat Politècnica de Valencia, Spain

SIGNAL 2024

Committee

SIGNAL 2024 Steering Committee

Wilfried Uhring, Université de Strasbourg, France
Jérôme Gilles, San Diego State University, USA
Constantin Paleologu, Polytechnic University of Bucharest, Romania
Sergey Y. Yurish, Excelera, S. L. | IFSA, Spain
Pavel Loskot, ZJU-UIUC Institute, China

SIGNAL 2024 Publicity Chairs

Sandra Viciano Tudela, Universitat Politecnica de Valencia, Spain
José Miguel Jiménez, Universitat Politecnica de Valencia, Spain

SIGNAL 2024 Technical Program Committee

Waleed H. Abdulla, The University of Auckland, New Zealand
Ahmed Al Hilli, Technical College of Najaf | Al-furat Al-Awsat Technical University, Iraq
Kiril Alexiev, Institute for Information and Communication Technologies -Bulgarian Academy of Sciences, Bulgaria
Djamila Aouada, SnT | University of Luxembourg, Luxembourg
Nadia Baaziz, Université du Québec en Outaouais, Canada
Junaid Baber, University of Balochistan, Pakistan
Vesh Raj Sharma Banjade, Intel Coporation, USA
Joan Bas, CTTC, Spain
Wassim Ben Chikha, Tunisia Polytechnic School, Tunisia
Amel Benazza-Benyahia, SUP'COM | COSIM lab. | University of Carthage, Tunisia
Anirban Bhowmick, Vellore Institute of Technology | Bhopal University, India
Larbi Boubchir, LIASD - University of Paris 8, France
Moez Bouchouicha, LIS - Laboratoire d'Informatique et Systèmes | Toulon University, France
Salah Bourennane, Ecole Centrale de Marseille, France
Geraldo Braz, Federal University of Maranhão, Brazil
Valeria Bruschi, Università Politecnica delle Marche, Ancona, Italy
Paula María Castro Castro, University of A Coruña, Spain
Aniruddha Chandra, National Institute of Technology (NIT), Durgapur, India
M. Girish Chandra, TCS Research & Innovation, India
Zhuyun Chen, South China University of Technology, Guangzhou, China
Doru Florin Chipper, Technical University Gheorghe Asachi of Iasi, Romania
Sergio Cruces, Universidad de Sevilla, Spain
João Dallyson Sousa de Almeida, Federal University of Maranhão, São Luís, Brazil
Natasja M. S. de Groot, Erasmus Medical Center | Technical University Delft, Netherlands
Laura-Maria Dogariu, University Politehnica of Bucharest, Romania
António Dourado, University of Coimbra, Portugal
Konstantinos Drossos, Tampere University, Finland
Hannes Fassold, JOANNEUM RESEARCH – DIGITAL, Graz, Austria

Laurent Fesquet, TIMA / Grenoble Institute of Technology, France
Sid Ahmed Fezza, National Institute of Telecommunications and ICT, Oran, Algeria
Óscar Fresnedo Arias, University of A Coruña, Spain
Faouzi Ghorbel, National School of Computer Science in Tunis | CRISTAL Laboratory, Tunisia
Mohammed Amine Ghrissi, Ministry of transport Algerian Civil Aviation authorities, Algeria
Gopika Gopan K, International Institute of Information Technology, Bangalore, India
Paul Irofti, University of Bucharest, Romania
Nobutaka Ito, Khon Kaen University, Thailand
Yuji Iwahori, Chubu University, Japan
Suresh K., Govt. Engineering College, Wayanad, India
Ahmad Karfoul, Université de Rennes 1, France
Ali Kariminezhad, Ruhr-Universität Bochum, Germany
Sokratis K. Katsikas, Center for Cyber & Information Security | Norwegian University of Science & Technology (NTNU), Norway
Csaba Kertész, University of Tampere / Neuroeventlabs Oy, Finland
Ted Kok, Canaan Semiconductor Ltd., Hong Kong
Jérôme Landré, Jönköping University, Sweden
Chih-Lung Lin, Hwa-Hsia University of Technology, Taiwan
Pavel Loskot, ZJU-UIUC Institute, China
Lisandro Lovisolo, State University of Rio de Janeiro (UERJ), Brazil
Francois Malgouyres, Institut de Mathématiques de Toulouse | Université Paul Sabatier - ANITI, France
Depu Meng, University of Michigan, Ann Arbor, USA
Zied Mnasri, Université de Tunis-El Manar, Tunisia
Sudipta Mukhopadhyay, Indian Institute of Technology, Kharagpur, India
Abdelkrim Nemra, Ecole Militaire Polytechnique, Algiers, Algeria
Wesley Nunes Gonçalves, Federal University of Mato Grosso do Sul, Brazil
Constantin Paleologu, University Politehnica of Bucharest, Romania
Thomas Paviet-Salomon, ISEN-Brest, France
Rodrigo Pereira Ramos, Federal University of São Francisco Valley (UNIVASF), Brazil
Jean-Christophe Pesquet, CentraleSupélec - Inria - University Paris-Saclay, France
Zsolt Alfred Polgar, Technical University of Cluj Napoca, Romania
Diogo Pratas, University of Aveiro, Portugal
J. K. Rai, Amity University Uttar Pradesh, Noida, India
Grzegorz Redlarski, Gdansk University of Technology, Poland
Aurobinda Routray, Indian Institute of Technology, Kharagpur, India
Diego P. Ruiz, University of Granada, Spain
Antonio-José Sánchez-Salmerón, Universitat Politècnica de València, Spain
Luiz Satoru Ochi, Instituto de Computação - UFF, Rio de Janeiro, Brazil
Lotfi Senhadji, Université de Rennes 1, France
Akbar Sheikh-Akbari, Leeds Beckett University, UK
Carlas Smith, TU Delft, Netherlands
Silvia F. Storti, University of Verona, Italy
Simron Thapa, Louisiana State University, USA
Laszlo Toth, University of Szeged, Hungary
Carlos M. Travieso-González, University of Las Palmas de Gran Canaria, Spain
Rajesh Kumar Tripathy, BITS Pilani, Hyderabad, India
Filippo Vella, National Research Council of Italy, Italy
Tengfei Wang, The Hong Kong University of Science and Technology (HKUST), Hong Kong

Yi-Chiao Wu, Nagoya University, Japan
Nelson Yalta, Hitachi R&D, Japan
Ching-Nung Yang, National Dong Hwa University, Taiwan
Nicolas H. Younan, Mississippi State University, USA
Rafal Zdunek, Wroclaw University of Science and Technology, Poland
Shuanghui Zhang, National University of Defense Technology, Changsha, China
Siwei Zhang, German Aerospace Center (DLR), Germany
Guanlong Zhao, Google, USA

Copyright Information

For your reference, this is the text governing the copyright release for material published by IARIA.

The copyright release is a transfer of publication rights, which allows IARIA and its partners to drive the dissemination of the published material. This allows IARIA to give articles increased visibility via distribution, inclusion in libraries, and arrangements for submission to indexes.

I, the undersigned, declare that the article is original, and that I represent the authors of this article in the copyright release matters. If this work has been done as work-for-hire, I have obtained all necessary clearances to execute a copyright release. I hereby irrevocably transfer exclusive copyright for this material to IARIA. I give IARIA permission to reproduce the work in any media format such as, but not limited to, print, digital, or electronic. I give IARIA permission to distribute the materials without restriction to any institutions or individuals. I give IARIA permission to submit the work for inclusion in article repositories as IARIA sees fit.

I, the undersigned, declare that to the best of my knowledge, the article does not contain libelous or otherwise unlawful contents or invading the right of privacy or infringing on a proprietary right.

Following the copyright release, any circulated version of the article must bear the copyright notice and any header and footer information that IARIA applies to the published article.

IARIA grants royalty-free permission to the authors to disseminate the work, under the above provisions, for any academic, commercial, or industrial use. IARIA grants royalty-free permission to any individuals or institutions to make the article available electronically, online, or in print.

IARIA acknowledges that rights to any algorithm, process, procedure, apparatus, or articles of manufacture remain with the authors and their employers.

I, the undersigned, understand that IARIA will not be liable, in contract, tort (including, without limitation, negligence), pre-contract or other representations (other than fraudulent misrepresentations) or otherwise in connection with the publication of my work.

Exception to the above is made for work-for-hire performed while employed by the government. In that case, copyright to the material remains with the said government. The rightful owners (authors and government entity) grant unlimited and unrestricted permission to IARIA, IARIA's contractors, and IARIA's partners to further distribute the work.

Table of Contents

Mixture Based Hybrid Regularization Method for Blind Image Deconvolution <i>Linghai Kong and Suhua Wei</i>	1
Fractional Order Variational Approach for Image Denoising and CT Reconstruction <i>Suhua Wei and Linghai Kong</i>	4
Feature Point Correction and Image Merging for Enhanced Branch Detection in Vineyard Drone Photography <i>YuJie Wu, Naoki Morita, Ashraf Naim Muhammad, and Kenta Morita</i>	6
Reconstruction of High-energy X-ray Source Using L-Cylinder Imaging Device <i>Haibo Xu, Ruogu She, and Xinge Li</i>	10
Paintings-100: A Diverse Painting Dataset for Large Scale Classification <i>Erica Knizhnik, Brian Rivera, Atreyee Sinha, and Sugata Banerji</i>	12
Evaluation of Multi-Angle System for Reflecting Piano Lessons <i>Md Saidi Muhammad Ashraf Naim, Naoki Morita, Kenta Morita, Chiharu Nakanishi, Chiaki Sawada, and Kazue Kawai</i>	16
Key Ideas in Parameter Estimation <i>Pavel Loskot</i>	18
Design of Third-Order Tensorial RLS Adaptive Filtering Algorithms <i>Ionut-Dorinel Ficiu, Camelia Elisei-Iliescu, Laura-Maria Dogariu, Constantin Paleologu, Cristian-Lucian Stanciu, and Cristian Anghel</i>	28

Mixture Based Hybrid Regularization Method for Blind Image Deconvolution

Linghai Kong, Suhua Wei

Institute of Applied Physics and Computational Mathematics
Beijing, China

email: kong_linghai@iapcm.ac.cn, wei_suhua@iapcm.ac.cn

Abstract—Following our recent work on mixed Poisson-White Spike noisy image restoration, we present a multi-convex optimization model to address the fundamental problem of Poisson blind image deconvolution (BID). This problem is encountered in a special application of X-ray radiography in hydro-tests, which also plays an important role in advanced tomographic imaging. We utilize a combined two-dimensional Square Cauchy-Gaussian distribution, whose parameters are totally unknown, to characterize the base structure of the convolution kernel. A new prior density function for the convolution kernel is proposed by integrating the structure density into a Kullback-Leibler divergence. The multi-convex optimization model is derived by a joint maximum a posteriori estimation (MAP) procedure, into which local estimation and expectation maximization algorithm are involved to gain convexity and solvability. To solve the proposed model numerically, a block coefficient descent based algorithm is to be proposed, in which majorization-minimization algorithm and Barzilai-Borwein estimation along with alternating direction minimization of multipliers are utilized to promote the computational efficiency. Numerical results show the effectiveness of our proposed algorithm, as well as its adaptivity.

Index Terms—Poisson blind image deconvolution; Square Cauchy distribution; Multidirectional fractional-order derivatives; Multi-convex; Combined 2-dimensional Square Cauchy-Gaussian distribution

I. INTRODUCTION

We consider a photon-limited BID problem encountered in a specific application of flash X/ γ -ray radiography (FXR) for hydrodynamic experiments [1] [2], which serves as crucial preprocessing in advanced FXR imaging, especially in 2-dimensional (2D) and 3-dimensional (3D) tomographic reconstruction. Till now, the existing methods of digital radiograph processing are commonly non-blind or based on known Gaussian kernel under the classical Gaussian noise assumption. In applications, however, due to physical and geometrical limitations of the digital radiography system, the acquired data suffer many types of perturbation other than the Gaussian ones. Besides a typically signal-dependent component, i.e., photon shot or Poisson noise [3]–[5], it is noteworthy that heavy-tailed very impulsive components must be taken into account for better understanding both the system blur and the noise as well [6], [7] and [4].

The rest of this submission is organized as follows. In Section 2, we present a new noisy degraded image model and then introduce briefly the modeling procedure of our proposed hybrid regularization model for Poisson BID. In Section 3, we

introduce in brief our main idea on how to solve the proposed model numerically. An experimental result is shown to validate our approach. More details on the numerical scheme and additional experimental results will be present on site. Section 4 concludes this submission.

II. PROPOSED MODEL

In applications, due to the type and amount of the contamination, it is difficult to present an accurate noise model, and most studies are built upon a common or oversimplified, *signal-independent* choice, i.e., additive white Gaussian noise. In this study, we pay more attention to two kinds of non-Gaussian perturbation. In fact, Poisson noise can be introduced to the intensity image by the counting process at the scintillator and the CCD array, which is a typical example of *signal-dependent* noise, and more familiar to fluorescence microscopy, positron emission tomography and astronomy. Moreover, a special case of impulsive behavior has to be considered. Indeed, there always exists a large number of radiation particles in high energy radiography, although not irradiated directly, reaching the CCD detector and contaminating the image. This perturbation can also be produced by secondary scattered neutron and gamma radiation hitting the detector even endowed with sophisticated shielding [8]. The struck pixels are displayed as white spikes, which are generally hold much bigger signal counts than those of neighboring pixels and more frequently observed in the dark or extremely low contrast areas.

A highly valued aspect of high energy radiography is the ability to resolve fine details in the high-density object, and resolution depends on the size of the radiographic source spot [9]. Various techniques and definitions have been proposed for measuring and characterizing the spot size at different laboratories, from which a general conclusion can be drawn that heavy-tailed distributions, including two-dimensional Cauchy distribution and Square Cauchy distribution, also known as Quasi-Bennett distribution and Bennett distribution [9], respectively, are more physically realistic than the Gaussian one to characterize the source spot, although their parameters are still very hard to measure or determine in good accuracy. It is shown in [10] that the Cauchy distribution and Gaussian distribution are of Lévy-stable type. On the other end, to model the detector response or simulate X-ray scattering in

X-ray radiography, it is notable that Cauchy distribution can also be deduced theoretically from the assumption of isotropic radiation [11].

In this section, we address the Poisson BID problem in the image space. We adopt the one-dimensional mixture of Poisson and Square Cauchy (MPsC) distributions [4] to characterize the noise in radiographic data, and extend the MPsC denoising method to address the Poisson BID problem. To better condition the deblurring process, our main idea is introducing a combined two-dimensional Square Cauchy-Gaussian distribution with unknown parameters to approximate the basal structure of the unknown blur kernel, and then, integrating it into a Kullback-Leibler (KL) divergence (see [4] and references therein) to construct our prior kernel density function.

Let $f, u, k, w, b : \Omega \rightarrow [0, 1]$ be the recorded noisy blurred image, the source image, the blur kernel, and the additive Square Cauchy noise, and the background, respectively. $\Omega = (-1, 1)^2$ denotes the image domain. In applications, one may assume that b is the mean of a known Poisson distribution. Assuming a convolution blur model for a linear radiographic system, we propose the following noisy degraded image model

$$f = \text{Poisson}(k * u + b) + w \doteq z(u, k) + w, \quad (1)$$

in which z is a realization of Poisson distributed random variable Z with PDF given by

$$P_Z^{U,K}(z; k * u + b) = \frac{(k * u + b)^z e^{-(k * u + b)}}{z!}, \quad (2)$$

k is the blur kernel, $*$ denotes the two-dimensional linear convolution operator, w is a realization of square Cauchy distributed random variable, whose PDF is given by $P_W(w; \sigma_w^2) = \frac{2\sigma_w^3}{\pi(\sigma_w^2 + |w|^2)^2}$, $\sigma_w^2 > 0, w \in \mathbb{R}$.

Proper formulations of both the latent image prior and the blur prior are crucial to the success of BID methods. In our context, the convolution kernel k is regarded as realization of a random variable \mathcal{K} , whose PDF is assumed to be unknown, except it can be characterized by a heavy-tailed mixture of Lévy-stable distributions [9] [10]. For convenience of discussion, in the follow we consider a combined 2-dimensional Square Cauchy-Gaussian distribution with PDF $B_k(x; \Theta_B) = \sum_{i=1}^2 \gamma_i p_i(x; \sigma_i^2)$, $x \in \Omega$ as prior structure of the kernel, where p_1 and p_2 are defined by

$$p_1(x; \sigma_1^2) = \frac{\sigma_1^2}{\pi(\sigma_1^2 + |x|^2)^2}, p_2(x; \sigma_2^2) = \frac{1}{2\pi\sigma_2^2} \exp\left(-\frac{|x|^2}{2\sigma_2^2}\right), \quad (3)$$

respectively, the denotation Θ_B represents the set of parameters $\gamma_1, \gamma_2, \sigma_1^2, \sigma_2^2$. $\gamma_i \geq 0$ is a mixture ratio satisfying $\gamma_1 + \gamma_2 = 1$.

We then utilize the KL divergence to measure the difference between the unknown kernel k and the basal structure $B_k(x; \Theta_B)$, and define a prior constraint on the blur kernel k given by $P_K(k) \propto e^{-J_K(k)}$ with

$$J_K(k)(x) = k(x)[\ln k(x) - \ln B_k(x; \Theta_B) - 1] + B_k(x; \Theta_B). \quad (4)$$

In terms of the prior constraint on the source image, we employ the combined first order TV and multidirectional FOTV of [12]–[14] to define a gradient's sparsity enhancing PDF of the source image, which is given in the Gibbs form as

$$P_U(u) \propto e^{-J_U(\nabla u, \nabla^\alpha u)}, J_U(\nabla u, \nabla^\alpha u) = g_1 |\nabla u| + g_2 |\nabla^\alpha u|, \quad (5)$$

where $\alpha \in (1, 2]$ denotes the order of multidirectional fractional-order derivatives in the Grünwald-Letnikov sense, $g_1(x)$ and $g_2(x)$ are defined as the same spatially adaptive functions in [4]. The multidirectional FOTV or FOTV4 [13] [4] is utilized to promote the selectivity of edges, and suppress more perturbation in the image as well.

Under these presumptions, our BID problem is then translated into recovering the latent image u and degradation kernel k from a single observation f with (1), (3), (4) and (5). Introduce denotation $\Theta = \{\sigma_w^2\} \cup \Theta_B$. In our context, we also assume that all the parameters in Θ are unknown.

III. NUMERICAL ALGORITHM IN BRIEF

Taking advantage of variational Bayesian and MAP principles, we will propose a multi-convex variational framework for the Poisson BID problem, into which an expectation maximization (EM) scheme is incorporated to estimate directly the parameters of the kernel structure as well.

In brief, we will report the modeling processes of the proposed variational Bayesian framework, in which some modifications, such as local approximation for the blur image and EM estimation for kernel structure parameters, are involved to gain solvability and convexity. Moreover, the convexity of the proposed optimization model is validated. As for the numerical algorithm for our proposed model, a block coefficient descent (BCD) [15] [16] based algorithm of the Gauss-Seidel type is to be present, in which majorization-minimization algorithm [17] [18] and Barzilai-Borwein estimation [19] along with alternating direction method of multipliers (ADMM) [20] are utilized to promote the computational efficiency. We use a localized structural similarity (SSIM) index to perform quantitative assessment on our methods.



Fig. 1. Left: A synthesized noisy blurred image. Center: A restored image by a comparison algorithm. Right: A restored image using our proposed algorithm.

Numerical results have shown the effectiveness of the proposed algorithm. In Figure 1, we present an example on BID, in which the left image is a synthesized noisy blurred image, obtained by convoluting with a combined Square Cauchy-Gaussian kernel and then adding a mixed Poisson-Cauchy

noise (SSIM=0.4581). The center image (SSIM=0.7275) is obtained by a comparison algorithm, or median filter injunction with a shock filter. The right one (SSIM=0.9407) is obtained by our proposed algorithm.

IV. CONCLUSION

A novel multi-convex optimization framework was proposed for blind deblurring images degraded by Lévy-stable blurs and contaminated by high-level non-Gaussian noises. Numerical results showed the effectiveness of the proposed algorithm on deblurring and denoising simultaneously, as well as adaptivity and quality. Learning based methods may be introduced in some future work to further promote the performance of our proposed method.

REFERENCES

- [1] R. Abraham, M. Bergounioux and E. Trelat, "A penalization approach for tomographic reconstruction of binary axially symmetric objects," *Appl. Math. Optim.* vol. 58, pp. 345–371, 2008.
- [2] M. Bergounioux, **et al.**, "Variational methods for tomographic reconstruction with few views," *Milan J. Math.* vol. 86, pp. 157–200, 2018.
- [3] D. L. Snyder, A. M. Hammoud and R. L. White, "Image recovery from data acquired with a charge-coupled-device camera," *J. Opt. Soc. Am. A.* vol. 10, pp. 1014–1023, 1993.
- [4] S. Wei and L. Kong, "A combined first and fractional order regularization method for mixed Poisson-White Spike noisy image restoration," *Inverse problems and imaging*. vol. 18, pp. 38–61, Feb 2024.
- [5] T. Le, R. Chartrand and T. J. Asaki, "A variational approach to reconstructing images corrupted by Poisson noise," *J. Math. Imaging Vis.* vol. 27, pp. 257–263, 2007.
- [6] C. Ekdahl, "Characterizing flash-radiography source spots," *J. Opt. Soc. Amer. A*. vol. 28, pp. 2501–2509, 2011.
- [7] A. S. Carasso, "Direct blind deconvolution," *SIAM J. Appl. Math.* vol. 61, pp. 1980–2007, 2001.
- [8] M. Matsubayashi, A. Tsuruno, T. Kodaira and H. Kobayashi, "High resolution static imaging system using a cooled CCD camera," *Nuclear Instruments and Methods in Physics Research A*, vol.377, pp. 107–110, 1996.
- [9] C. Ekdahl, "Characterizing flash-radiography source spots," *J. Opt. Soc. Amer. A*. vol. 28, pp. 2501–2509, 2011.
- [10] A. S. Carasso, "Direct blind deconvolution," *SIAM J. Appl. Math.* vol. 61, pp. 1980–2007, 2001.
- [11] K. M. Hanson, "Introduction to Bayesian image analysis," In: *Image Processing, Proc. SPIE 1898* (ed. M. H. Loew), pp. 716–731, 1993.
- [12] J. Bai and X.-C. Feng, "Fractional-Order anisotropic diffusion for image denoising," *IEEE Trans. Image Proc.* vol. 16, pp. 2492–2502, 2007.
- [13] Q. Liu and S. Gao, "Directional fractional-order total variation hybrid regularization for image deblurring," *J. Electron. Imaging*. vol. 29, pp. 033001, 2020.
- [14] J. Zhang and K. Chen, "A total fractional-order variation model for image restoration with nonhomogeneous boundary conditions and its numerical solution," *SIAM J. Imaging Sciences*. vol. 8, pp. 2487–2518, 2015.
- [15] Y. Xu, "Block Coordinate Descent for regularized multi-convex optimization," MA thesis, Rice University, Houston, Texas, 2013.
- [16] Y. Xu and W. Yin, "A block coordinate descent method for regularized multiconvex optimization with applications to nonnegative tensor factorization and completion," *SIAM J. Imaging Sci.* vol. 6, pp. 1758–1789, 2013.
- [17] D. Hunter and K. Lange, "A tutorial on MM algorithms," *The Amer. Statist.* vol. 58, pp. 30–37, 2004.
- [18] D. Perrone and P. Favaro, "A logarithmic image prior for blind deconvolution," *Int. J. Comput. Vis.* vol. 117, pp. 159–172, 2016.
- [19] O. Burdakov, Y. Dai and N. Huang, "Stabilized Barzilai-Borwein method," *J. Comput. Math.* vol. 37, pp. 916–936, 2019.
- [20] D. Gabay, "Applications of the method of multipliers to variational inequalities," in *Augmented Lagrange Methods: Applications to the solution of boundary-valued problems*, M. Fortin, R. Glowinski, Eds. North Holland, Amsterdam, 1983, 299–331.

Fractional Order Variational Approach for Image Denoising and CT Reconstruction

Suhua Wei
*Institute of Applied Physics and
 Computational Mathematics*
 Beijing, China
 email: wei_suhua@sina.com

Linghai Kong
*Institute of Applied Physics and
 Computational Mathematics*
 Beijing, China
 email: kong_linghai@iapcm.ac.cn

Abstract—Image denoising is a fundamental problem in the area of image processing. The widely applications make it very important to research. Variational method is an efficient way to restore images corrupted by noises. In this paper, we propose a variational model to deal with Gaussian noise and mixed noise. In the proposed model, we use the combination of Total Variation (TV) and Fractional order Total Variation (FTV) as the regularization term. Numerical results show that the proposed model has advantages on recovering image edges and textures. We also generalize our approach to CT image reconstruction by fan beam X-rays from a single radiograph. By a single radiograph, we can reconstruct an axially symmetric object image. The variational model and the algorithm to solve it will be given, and the efficiency of the proposed method will be illustrated by numerical tests.

Index Terms—image denoising; total variation; fractional order; CT; image reconstruction

I. INTRODUCTION

Image denoising is a fundamental problem that has been researched for a long time and yet no clear cut solution exists due to its ill-posedness. To overcome the ill-posedness of the inverse problem arised in image restoration, Total Variation (TV) regularization model was proposed by Rudin, Osher and Fatemmi in 1992 [5]. Since then, variational method was rapidly developed and widely used in image processing tasks. Various variational models were developed for image denoising, deblurring, segmentation, registration and so on. In this work, we focus on image denoising techniques and applications. Total variation regularization model is very efficient on recovering image edges while removing noises. But it often leads to staircase effects on the flat region, and small details, such as textures are often filtered out with noise. Therefore, the improved variational models were considered. Fractional order Total Variation (FTV) regularization has shown its advantages on texture preserving in recent research [1]-[4][6]. In this paper, we propose a new variational model by taking the combination of TV and FTV as regularizer for image noise removal. The proposed variational model is established according to noise type and its characteristics. The noise type deals with Gaussian noise and mixed Poisson and White Spike noise. We also construct the numerical algorithm for proposed model based on Alternating Direction Method of Multipliers (ADMM). Numerical tests show the effectiveness of the proposed method.

The rest of the short paper is organized as follows: In section 2, we describe the image denoising problem. The mathematical model and algorithm for eliminating Gaussian noise are given. In section 3, we introduce the CT image reconstruction. For axially symmetric objects reconstruction, we illustrate how to establish optimization problem by using the hybrid regularization of TV and FTV for getting efficient reconstruction while suppressing noise. In section 4, we give conclusions and future work.

II. IMAGE DENOISING

Generally, the process of image contaminated by Gaussian noise can be modeled as follows:

$$f = u + n \quad (1)$$

where f is the measured image contaminated by noise n , u is the true image to be recovered. The variational model for image denoising is composed of two parts, the first part is the data fitting term, the second part is the regularization term. The data fitting term depends on the noise type, and the regularization term utilizes the prior knowledge of the unknown image. Therefore, the restoration process results in the model:

$$\min_u \left\{ \frac{1}{2} \|u - f\|_2^2 + \mu \mathcal{R}(u) \right\}, \quad (2)$$

where μ is the regularization paprameter which balance the data fitting and regularizing. The choice of the regularization term is the key point of the model. For better recovery of the image edges and textures, we propose to use the hybrid regularization of TV and FTV, it takes the following form:

$$\mathcal{R}(u) = \int_{\Omega} g(x, y) |\nabla u| dx dy + \int_{\Omega} (1 - g(x, y)) |\nabla^{\alpha} u| dx dy \quad (3)$$

Why do we choose the combination of TV and FTV ? As we know, TV regularization is good at edge detection after image restoration, but smears small textures in some region. FTV regularization can protect image textures after restoration. The purpose of taking the combination of TV and FTV as regularizers is to have both advantages of TV and FTV. To balance the weight of TV and FTV, we use a gradient related functional g to judge edges and textures.

We will discuss how to choose fractional order α and the gradient related functional g . To solve the proposed model,



Fig. 1. Left is a clean image, middle is the noisy one, right is the denoised by our proposed model.

we use Alternating Direction Method of Multipliers. In Figure 1, we give an example of image denoising by our proposed model. The left image is clean, the middle is a noisy one contaminated by Gaussian noise, and the right is the denoised image by our proposed model. We add Gaussian noise to the clean image (left), then we get the noisy image (middle). We use the proposed model (2) to calculate the denoised image denoted by u . In equation (2), f represents the noisy image which is known. The numerical result u is the right image. We can see that the denoised image has got improvement on SNR (signal to noise ratio) and details recovery. For example the hair and the hat edges in Lena image.

III. CT RECONSTRUCTION

The image denoising idea can be extended to CT image reconstruction. As we know, CT image reconstruction is very helpful to diagnose the inner features of objects and characteristics of human bodies through x-ray radiographs. In this case, we talk about image reconstruction of axially symmetric objects from a single radiograph by fan beam x-ray. This leads to Abel transform inversion. Suppose the projection matrix is known A , the measured projection data is \mathbf{d} , and the object features to be solved is represented by ρ , the CT reconstruction is described by the following mathematical model:

$$\min_{\rho} \left\{ \frac{1}{2} \|A\rho - \mathbf{d}\|_2^2 + \mu \mathcal{R}(\rho) \right\}, \quad (4)$$

$$\mathcal{R}(\rho) = \int_{\Omega} g(r) |\nabla \rho| dr + \int_{\Omega} (1 - g(r)) |\nabla^{\alpha} \rho| dr \quad (5)$$

Where the function ρ is dependent on variable r which represents the radius of objects with axially symmetry.

CT image reconstruction is an important area for approaching. Especially when the noise type are mixed or even unknown, the reconstruction problem are challenging on mathematical modelling and numerical algorithm designing. If the optimization problem are not convex, there is no guarantee for the global solution of the optimization problem to be reached.

IV. CONCLUSIONS

We make an approach on image denoising variational models and algorithms. To deal with the ill-posedness of the

inverse problem, we introduce a new regularization term which combines the advantages of TV and FTV. This regularization technique has been applied to CT image reconstruction. For mixed poisson and white spiky noise, we have also explored image restoration models and numerical algorithms. Numerical experiments are given to show the efficiency of our proposed model on recovering image edges and textures while suppressing noises [1]. In the future, we will do further approach according to reviewers' suggestions. At the present stage, our research work is still going on, especially comparisons with other works will be illustrated through numerical tests.

ACKNOWLEDGMENT

This work is partially supported by National Natural Science Foundation of China (NSFC) under Grant Numbers 11571003,12271053.

REFERENCES

- [1] S. Wei, L. Kong, "A Combined First and Fractional Order Regularization Method for Mixed Poisson-White Spike Noisy Image Restoration," *Inverse Problems and Imaging*, vol. 18, pp.38–61, February 2024.
- [2] Z. Guo, W. Yao, J. Sun and B. Wu, "Nonlinear Fractional Diffusion Model for Deblurring Images with Textures," *Inverse Problems and Imaging*, vol. 13, pp.1161–1188, 2019.
- [3] M. R. Chowdhury, J. Zhang, J. Qin, Y. Lou, "Poisson image denoising based on fractional-order total variation," *Inverse Problems and Imaging*, vol. 14, pp.77–96, 2020.
- [4] J. Bai, X.-C. Feng, "Fractional Order anisotropic diffusion for image denoising," *IEEE Trans. Image Processing*, vol.16, pp.2492-2502, 2007.
- [5] L. Rudin, S. Osher, E. Fatemi, "Nonlinear total variation based noise removal algorithms," *Physica D*, vol.60, pp.259–268, 1992.
- [6] J. Zhang, K. Chen, "A total fractional-order variation model for image restoration with non-homogeneous boundary conditions and its numerical solution," *SIAM J. Imaging Sci.*, vol. 8, pp.2487–2518, 2015.
- [7] R. Abraham, M. Bergounioux and E. Trelat, "A penalization approach for tomographic reconstruction of binary axially symmetric objects," *Applied Mathematics and Optimization*, vol. 58, pp.345–371, 2008.
- [8] F. F. Dong and Y. M. Chen "A fractional-order derivative based variational framework for image denoising," *Inverse Problems and Imaging*, vol. 10, pp.27–50, 2016.

Feature Point Correction and Image Merging for Enhanced Branch Detection in Vineyard Drone Photography

YuJie Wu, Naoki Morita, Md Saidi Muhammad Ashraf Naim
 School of Information and Telecommunication Engineering
 Tokai University
 Tokyo, Japan

e-mail: wjl13357889606@gmail.com, wv062303@tsc.u-tokai.ac.jp, 0cjt2118@cc.u-tokai.ac.jp

Kenta Morita
 Faculty of Medical Engineering
 Suzuka University of Medical Science
 Mie, Japan
 e-mail: morita@suzuka-u.ac.jp

Abstract—This paper presents a new method for feature point correction and image merging in drone-based vineyard photography, aimed at improving branch detection accuracy. Addressing the issue of inaccurate feature point matching in traditional methods, we developed a technique that analyzes tangent angles between feature points, focusing on parallel alignment for precise merging. Our approach significantly enhances the accuracy of merged images, achieving about 90% precision compared to less than 10% in conventional methods. This advancement offers a promising solution for precise vineyard monitoring and management through aerial imagery.

Keywords- aerial image stitching; feature point correction; agricultural monitoring

I. INTRODUCTION

Monitoring the growth of branches in Japanese viticulture is crucial for harvesting tastier grapes and managing nutrients [1]. However, observing these branches from the ground is challenging. To overcome this limitation, we propose using drones for aerial monitoring of the branches.

In drone-based vineyard photography, shadows cast by the branches vary depending on the shooting location, leading to areas of high contrast and overlapping images where shadows merge. To address this issue, we proposed a method to eliminate the influence of shadows and enable the overlapping of branches in the images [2]. This method involves generating images that extract only the branches from aerial photographs and identifying key features from these images to facilitate merging (see Figure 2).

While this method was effective for images with varying shadow projections, there were instances where accurately extracting the necessary features for merging from the branch-only images proved challenging, resulting in excessive image distortion. As a result, merged images that displayed all branches extending from the trunks could not be produced.

Traditional image fusion methods have limitations in addressing this specific challenge. These methods fail to account for the complexities introduced by shadows and the

merging of branch images. Therefore, we propose a new method for feature point correction and image merging tailored specifically for aerial photographs of vineyards. By analyzing tangent angles between feature points and selecting the most parallel lines, our method aims to improve the accuracy of merged images.

To provide a comprehensive overview of the challenges in this field, it is essential to review existing literature. In the following section, we will discuss the problem statement, the significance of the problem, previous research outcomes, and how our proposed solution differs. This comprehensive literature review will shed light on the novelty and effectiveness of our proposed method.

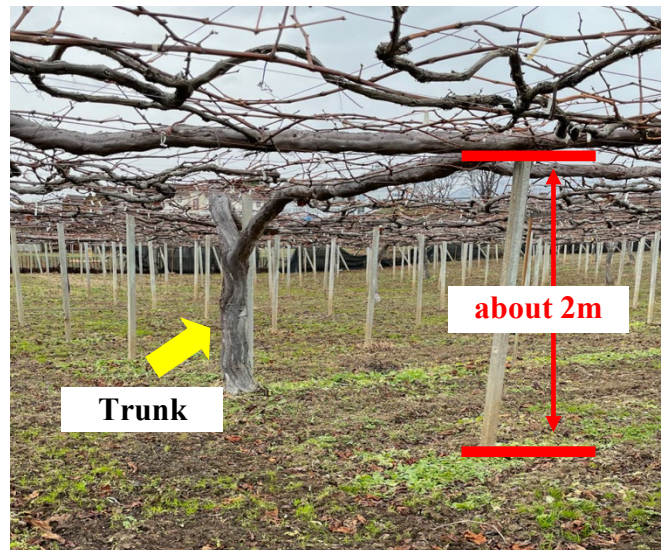


Figure 1. Photograph of the farm

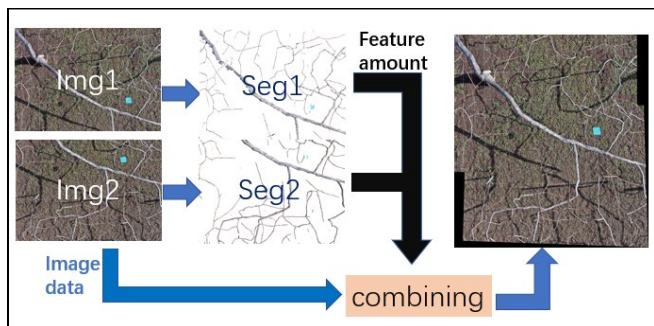


Figure 2. Method Proposed in Previous Research

The remainder of this paper is organized as follows: Section II discusses the problems with the conventional method. Section III outlines the objectives of this study. Section IV describes the proposed solution. Section V presents the experiments conducted, along with the results and discussion, and Section VI concludes the paper.

II. PROBLEM

This section introduces an analysis of feature point pairing in overlapping aerial photographs, crucial for accurate image stitching and analysis in precision agriculture. We begin with Figure 3, which illustrates the methodology for identifying and pairing feature points across overlapping images. Figure 3 displays pairs of feature points from overlapping aerial photographs. As can be seen in Figure 3, the feature points are paired one-to-one. However, in the same location as depicted in Figure 3, Figure 4 shows pairs of feature points from images that recognize only the branches. In Figure 4, there are several locations where the feature points are one-to-many. Despite areas that do not overlap being excluded from feature point extraction, they are still extracted as feature point pairs.

When these images are merged based on this information, the result, as shown in Figure 5, does not maintain the original form and is misplaced. Furthermore, beyond this point, additional image merging becomes impossible. Consequently, this prevents the accurate capture of the exact location and growth status of all branches extending from the trunk.



Figure 3. Feature Point Pairs from Two Overlapping Aerial Photographs

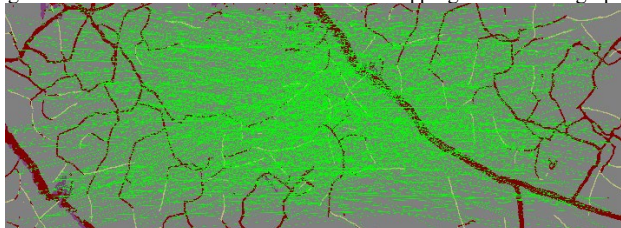


Figure 4. Feature Point Pairs from Recognition Images Showing Only Branches

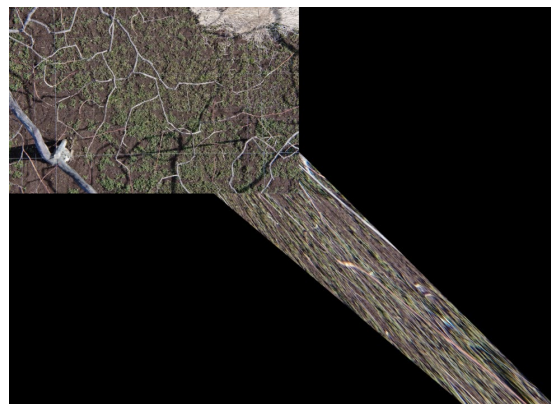


Figure 5. Merging Result Using Feature Point Pairs from Figure 4

III. PROPOSAL

When merging images using only translational movement, the feature point pairs of overlapping images become parallel. Our preliminary analysis of relevant images demonstrated that adjusting them through translational movement alone sufficiently aligned the branches. Exploiting this characteristic, our proposed method identifies the correct feature point pairs by selecting the line with the highest number of parallel feature point pairs and discards any other feature point tangents. This ensures that only the correct feature point pairs are used for merging.

While existing research on feature point correction, as referenced in [3] to [9], suggests various methods, the unique characteristic of our study, where translational movement alone is sufficient for merging, renders those methods unnecessary. Moreover, the feature point matching in the relevant feature point pairs for our research is prone to errors, making it challenging to apply conventional methods. Therefore, we propose a novel method specifically tailored for aerial photographs of vineyards, which addresses these limitations.

Compared to traditional methods, our proposed method offers distinct advantages. Firstly, it leverages the inherent characteristic of translational movement for merging, reducing the computational complexity and eliminating the need for complex algorithms employed in other methods. This simplifies the merging process and improves efficiency. Secondly, by selecting the feature point pairs with the most parallel lines, our method ensures more accurate alignment of branches in the merged images. This results in improved visual clarity and facilitates better analysis of the branches' growth patterns.

In practical applications, our method provides valuable benefits. Its simplicity and efficiency make it suitable for large-scale vineyards, where monitoring a vast number of branches can be time-consuming. By accurately merging images and extracting key features, our method enables more precise monitoring of the number of new shoots growing from the grapevine trunks. This information is crucial for optimizing grape quality and nutrient management. Furthermore, the proposed method can be easily integrated into existing drone-based monitoring systems, offering a practical solution for vineyard management.

In summary, our proposed method introduces a novel approach to feature point correction and image merging for aerial photographs of vineyards. By leveraging the inherent characteristic of translational movement and selecting the most parallel feature point pairs, our method improves the accuracy and efficiency of merge.

The objective of this research is to merge images in such a way that the branches extending from the trunk can be clearly identified. Specifically, if the feature point pairs extracted from recognition images are incorrect, the goal is to detect and eliminate them, thus ensuring that only correct feature point pairs are used for merging.

IV. EXPERIMENTS AND CONSIDERATIONS

This study aims to improve the merging of images at the boundary areas of branches in agricultural photography conducted by drones. We compared the merging rates of branches at the boundaries using both the conventional and proposed methods, summarizing and discussing the results.

A. Experimental Method

We merged images of all branches extending from the trunk individually and examined how many branches were misaligned at the image boundaries.

The misalignment was measured in terms of the thickness of the branches. Based on four datasets of trunk images, we analyzed the number of seamlessly merged branches and the number of branches that were separated by various distances (1-2 branches, 3-4 branches, and more). We then calculated the success rate of branch merging for each dataset.

Incorporating the findings from the preliminary investigation, we found that the necessary adjustments for accurate image merging, specifically rotations up to 0.8 degrees and resizing within a 6% margin, are well within the range that maintains feature point pairs in parallel alignment. This insight led to refining our method to better accommodate the slight deviations caused by drone vibrations, without sacrificing the precision of branch alignment in merged images.

We adjusted the tolerance for angle deviation to plus or minus 0.5 degrees, a strategic decision that not only addresses the challenges of drone flight dynamics but also harnesses the robustness of the SIFT algorithm for precise feature matching. This modification significantly improves the merging accuracy of branch images at boundaries, enhancing seamless integration and reducing misalignments.

This optimized approach underlines our commitment to advancing image processing techniques in agricultural monitoring. By adapting our methodology to the nuances of drone-captured imagery, we demonstrate the potential of sophisticated image processing to improve the accuracy and reliability of agricultural data collection, setting the stage for the detailed experimental results and analysis that follow in this section.

B. Experimental Results

1) *Table I:* Results by the Conventional Method shows the severe limitations of the conventional approach, with a

majority of branches misaligned and merging rates disastrously low.

2) *Table II:* Results by the Proposed Method illustrates the effectiveness of the proposed method, with nearly all branches aligned correctly and high merging rates across all datasets.

The experimental results are presented in two tables comparing the conventional method with the proposed method for merging images of vineyard branches. The tables quantify the alignment of branches in merged images, displaying the number of branches with varying degrees of misalignment and the overall merging rate. For the conventional method, the merging rate is notably low (below 10%), indicating a significant misalignment of branches. Conversely, the proposed method shows a substantial improvement, with the majority of branches exhibiting no misalignment and the merging rates increasing to approximately 90%. This demonstrates the effectiveness of the proposed method in improving the accuracy of image merging in agricultural photography conducted by drones, specifically in the context of vineyard monitoring.

TABLE I. RESULTS BY THE CONVENTIONAL METHOD

Trunk No.	No Misalignment	1-2 Branches	3-4 Branches	More	Merging Rate
1	14	47	54	67	7.69%
2	21	128	68	105	6.52%
3	21	97	50	109	7.58%
4	24	104	77	122	7.33%

TABLE II. RESULTS BY THE PROPOSED METHOD

Trunk No.	No Misalignment	1-2 Branches	3-4 Branches	More	Merging Rate
1	159	10	6	7	87.36%
2	310	3	8	1	96.27%
3	269	4	2	2	97.11%
4	313	3	3	8	95.72%

C. Analysis of Results

The results show that the merging accuracy of the proposed method, at around 90%, was significantly higher compared to less than 10% for the conventional method. The proposed method successfully merged many branches, demonstrating its effectiveness. However, there remains a need for further improvement to address the issue of some branches that still break apart, which is a challenge for future research.

V. CONCLUSION

The goal of this research was to merge images in a way that allows for the clear identification of branches extending from the trunk. We addressed the issue of distorted merged images caused by incorrect feature point pairs in recognition images that only retain branches. To this end, we reconsidered the method of selecting feature point pairs and proposed a new method of image merging using tangent angles. This new approach significantly reduced feature point mismatches,

improving the merging accuracy from less than 10% with the conventional method to approximately 90% with the proposed method. This demonstrates the effectiveness of the proposed method.

In the future, we aim to solve the remaining issues with broken branches and achieve even higher precision in image merging.

REFERENCES

- [1] Y. Nirasaki-shi CUPOD FARM [Online]. Available from: <https://www.cupidfarm.co.jp/> [accessed: 2023-12-1]
- [2] Y. J. Wu, M. Wakao, N. Morita, and K. Morita, "A Method for Removing Shadows from Photos Taken with a Drone and Stitching the Photos Together," in Proceedings of the GEOProcessing 2023: The Fifteenth International Conference on Advanced Geographic Information Systems, Applications, and Services, 2023, pp. 56-60.
- [3] L. Y. Tian, R. Hu, B. Yang, S. Liu, L. Yin, and W. Zheng, "Improved Feature Point Pair Purification Algorithm Based on SIFT During Endoscope Image Stitching," *Frontiers in Neurorobotics*, vol. 16, 2022.
- [4] Z. Jiang, Z. Zhang, X.-Y. Fan, and R. Liu, "Towards All Weather and Unobstructed Multi-Spectral Image Stitching: Algorithm and Benchmark," *ACM Transactions on Multimedia Computing, Communications, and Applications*, 2021.
- [5] Y. Mo, X. Kang, P. Duan, and S. Li, "A Robust UAV Hyperspectral Image Stitching Method Based on Deep Feature Matching," *IEEE Transactions on Geoscience and Remote Sensing*, 2021.
- [6] J. Chen, Z.-C. Li, C. Peng, Y. Wang, and W. Gong, "UAV Image Stitching Based on Optimal Seam and Half-Projective Warp," *Remote Sensing*, vol. 14, no. 5, 1068, 2022.
- [7] Q. Wei and X. Li, "Two Degree of Freedom Dynamic Model Parameter Identification of Accelerometer Using Feature Point Coordinate Estimation and Amplitude Correction," *Journal of Advanced Computational Intelligence and Intelligent Informatics*, vol. 26, no. 5, pp. 965-973, 2022.
- [8] M. Liu, Y. Han, X. Xi, S. Tan, J. Chen, L. Li, and B. Yan, "Thermal Drift Correction for Laboratory Nano Computed Tomography via Outlier Elimination and Feature Point Adjustment," *Sensors*, vol. 21, no. 24, 8493, 2022.
- [9] C. Yao, H. Zhang, J. Zhu, D. Fan, Y. Fang, and L. Tang, "ORB Feature Matching Algorithm Based on Multi-Scale Feature Description Fusion and Feature Point Mapping Error Correction," *IEEE Access*, 2023.

Reconstruction of High-energy X-ray Source Using L-Cylinder Imaging Device

Haibo Xu

*Institute of Applied Physics and
Computational Mathematics
Beijing, P. R. China*

Email: xu_haibo@iapcm.ac.cn

Ruogu She

*Institute of Applied Physics and
Computational Mathematics
Beijing, P. R. China*

Email: she_ruogu@iapcm.ac.cn

Xing Li

*Institute of Applied Physics and
Computational Mathematics
Beijing, P. R. China*

Email: li_xing@iapcm.ac.cn

Abstract—The L-Edge and L-Cylinder imaging devices are used to reconstruction the image of high-energy X-ray source. The physical model considering the penetration effect of X-ray to the imaging device is established, the transmission imaging matrix is constructed, and the algebraic solution method of spot image reconstruction is established. The X-ray source with Gaussian distribution is reconstructed. The results show that the artifacts and discontinuous in the center of the reconstructed images can be improved using L-Cylinder imaging device.

Index Terms—reconstruction, X-ray source, L-Cylinder

I. INTRODUCTION

The blur caused by the high energy X-ray source spot is one of the important factors leading to image degradation. Focal spot measurement is an important part of studying high-energy X-ray flash radiography. The major laboratories engaged in the research of high-energy X-ray flash radiography at home and abroad have carried out the related research on spot size measurement, and representative methods include pinhole method, slit method, edge method, rollbar method and so on.

In 2016, Fowler et al. [1] designed the L-Rolled Edge device for imaging based on the "opaque" physical model of the imaging device proposed by Barnea [2], using only one corner of the square hole imaging device, obtained the imaging light and shade information of two dimensions, and gave the two-dimensional intensity distribution of focal spot through image reconstruction. In this paper, based on the "L" configuration device, an imaging physical model considering transmission effect is proposed, and L-Cylinder imaging device is used to reconstruct the X-ray source image. The two-dimensional distribution of the source penetrating the imaging device is obtained, and the intensity distribution of the source is derived by image reconstruction.

An outline of the rest of the paper is as follows. In Section 2, We present the physical model and solution method. Numerical results for reconstruction using L-Cylinder imaging device are presented in Section 3. Finally, the conclusion are summarized in Section 4.

II. PHYSICAL MODEL AND SOLUTION METHOD

It is assumed that the X-ray source is an ideal source, that is, an isotropic monomeric point source. The intensity of X-

rays emitted from the source, passing through the object and reaching each point on the detector plane can be expressed as

$$I(x, y) = I_0(x, y)e^{-L(x, y)} = I_0(x, y)e^{-\int_0^{d(x, y)} \mu(l)dl}, \quad (1)$$

where $I(x, y)$ and $I_0(x, y)$ are the intensity of X-rays received by the detector with or without objects, $L(x, y)$ is the total optical path of the X-rays to point (x, y) on the imaging plane, $d(x, y)$ is the distance from the point (x, y) on the imaging plane to the source, and $\mu(l)$ is the linear attenuation coefficient of X-rays in the material at a distance l from the source.

If the source plane and the imaging plane are respectively discretized in pixels and regarded as one-dimensional vectors, the formula 1 can be written in the form of matrix multiplied by vector:

$$\mathbf{Ax} = \mathbf{b}, \quad (2)$$

where \mathbf{b} is the measurement vector, \mathbf{x} is the reconstructed image vector, and \mathbf{A} is the projection matrix of size $M \times N$. The element a_{ij} of matrix \mathbf{A} reflects the overall attenuation of the i -th source intensity reaching the j -th pixel in the imaging plane after passing through the imaging device. In practice, if noise generally exists, the above formula becomes

$$\mathbf{Ax} = \mathbf{b} + \mathbf{n}, \quad (3)$$

where \mathbf{n} is the noise of the imaging system.

It is assumed that the source is 15cm away from the center of L-Edge and the imaging plane is 120cm away from the center of L-Edge, that is, the geometric magnification ratio M of the imaging system is 8. Assuming that the L-Edge imaging device is a homogeneous single medium, the element a_{ij} of the imaging matrix based on the transmission model can be written as

$$a_{ij} = I_0 e^{-L((x', y') \rightarrow (x, y))} \quad (4)$$

where $L((x', y') \rightarrow (x, y))$ is the optical path of X-rays passing through the L-Edge imaging device on the path from point (x', y') in the source plane to point (x, y) in the imaging plane. It can be derived according to the geometric relative position relationship.

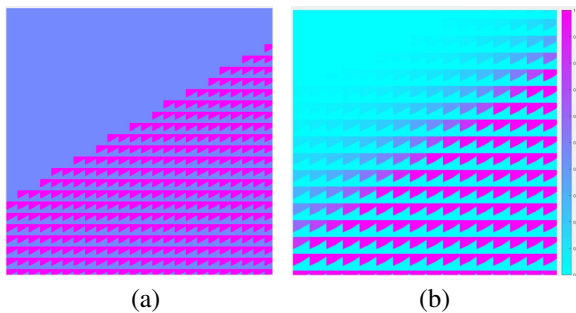


Fig. 1. Imaging matrix of L-Edge imaging device with different physical models (local enlargement). (a) Opaque model; (b) Transmission model considering transmission effect.

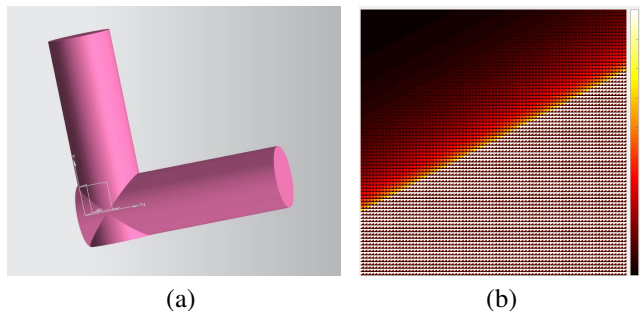


Fig. 2. (a) L-Cylinder imaging device; (b) The transmission imaging matrix of the L-Cylinder device.

For the "opaque" model adopted by Barnea et al. [2], it is equivalent to μ being infinity, and the matrix element based on the "opaque" model can be written as:

$$a_{ij} = \begin{cases} 1, & L > 0, \\ 0, & L = 0. \end{cases} \quad (5)$$

Figure 1 shows the imaging matrix of these two models under the same imaging state. It can be seen that the transition between light and shade of opaque model is simple, see Figure 1(a), whereas the imaging matrix in Figure 1(b) changes gradually after considering the transmission effect, which can more truly reflect the gradual change of X-ray intensity when penetrating L-Edge imaging device.

III. RECONSTRUCTION OF SOURCE

In view of the right angle edge of L-Edge imaging device, there is a sudden change of image intensity near the edge, which leads to serious artifacts in the reconstructed image [3]. Therefore, we propose an improved design, that is, the L-Cylinder imaging device is directly formed by splicing two sections of cylinders into an "L" shape, as shown in Figure 2(a). The transmission imaging matrix of the constructed L-Cylinder device is shown in Figure 2(b). The transmission imaging matrix based on the improved imaging device can form a uniform band transition region, which is beneficial to the smoothness of the reconstructed image theoretically.

Set the FWHM of X-ray source with Gaussian distribution used in the Monte Carlo simulation as 0.2 cm. Figure 3 shows the MC photographic image of this source and its reconstructed intensity distribution, and the cross-sectional

lines of the reconstructed image in different directions are shown in Figure 4 [4].

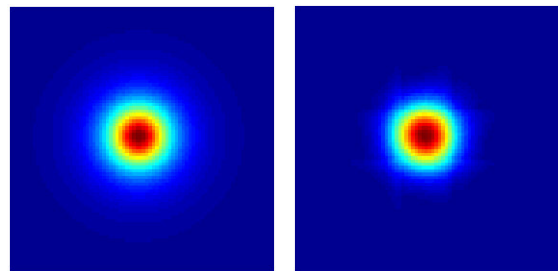


Fig. 3. Ground truth and reconstruction of Gaussian Source. Left: Ground truth; Right: Reconstruction with L-Cylinder device.

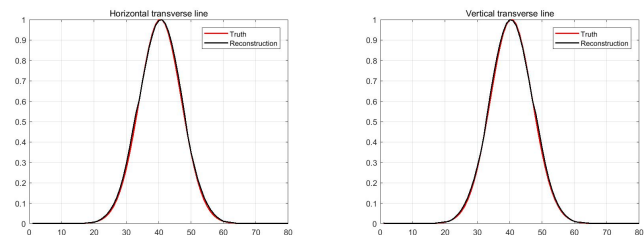


Fig. 4. Transverse lines of reconstructed source in horizontal and vertical directions.

As can be seen from Figure 4, the L-Cylinder imaging device can well reconstruct the intensity distribution of Gaussian source, and accurately measure the FWHM of Gaussian source to be 0.2cm. The L-Cylinder imaging device significantly improves the discontinuity phenomenon which reconstructed with L-Edge imaging device.

IV. CONCLUSION

In this paper, the spot measurement method of high-energy X-ray source based on image reconstruction is studied. The physical model considering the penetration effect of X-ray to the imaging device is established, and the algebraic solution method of spot image reconstruction is established. The X-ray source with Gaussian distribution is reconstructed. The results show that the artifacts and discontinuous in the center of the reconstructed images can be improved using L-Cylinder imaging device, and is more suitable for the reconstruction of high-energy X-ray source.

REFERENCES

- [1] M. J. Fowler, M. Howard, A. Luttmann, S. E. Mitchell, and T. J. Webb, "A stochastic approach to quantifying the blur with uncertainty estimation for high-energy X-ray imaging systems", *Inverse Problems in Science and Engineering*, vol.24, pp.353-371, Mar. 2016.
- [2] G. Barnea, "Penumbral imaging made easy", *Review of Scientific Instruments*, vol.65, pp.1949-1953, Jun. 1994.
- [3] A. E. Schach von Wittenau, C. M. Logan, and R. D. Rikard, "Using a tungsten rollbar to characterize the source spot of megavoltage bremsstrahlung linac", *Medical Physics*, vol.29, pp.1797-1806, Aug. 2002.
- [4] H. Xu, Y. Hu, S. Wei, "Quantitative simulation and density reconstruction in high-energy X-ray radiography", *Chinese Journal of Computational Physics*, vol.28, pp.906-914, Nov. 2011.

Paintings-100: A Diverse Painting Dataset for Large Scale Classification

Erica M. Knizhnik^{*†}, Brian Rivera^{*‡}, Atreyee Sinha[§], and Sugata Banerji^{*¶}

^{*}Department of Mathematics and Computer Science, Lake Forest College, Lake Forest, IL, USA.

[†]Email: knizhnikem@lakeforest.edu

[‡]Email: riverab@lakeforest.edu

[§]Computing and Information Sciences, Edgewood College, Madison, WI, USA. Email: asinha@edgewood.edu

[¶]Corresponding author. Email: banerji@lakeforest.edu

Abstract—Painting classification is an interesting cross-disciplinary research problem in computer vision. With the increased accessibility of digitized collections of fine-art paintings, development of effective painting classification algorithms has become vital as they have many potential applications in museums, various industries, painting theft investigation, forgery detection, art education, etc. However, the availability of large scale annotated benchmark datasets with high-resolution authentic painting images still remains a challenge. Towards that end, in this work, we develop an image dataset consisting of high-resolution painting images from 100 different artists spanning 14 different styles. This dataset is an extension of the Painting-91 dataset constructed by Khan et al. Our contribution towards extending this dataset are threefold. First, we address the limitations of the dataset by removing errors and enhancing image resolutions. Second, we add more images to augment some of the artist categories with fewer images. Third, we include the works of nine more painters from diverse backgrounds and styles for creating a more representative and inclusive database of fine-art paintings. We also perform a preliminary evaluation of this newly constructed Paintings-100 dataset using several different Convolutional Neural Network (CNN)-based classification techniques for artist recognition. Furthermore, we demonstrate that our proposed and improved dataset is more suitable for patch-based models than the earlier published Painting-91 dataset due to larger image resolutions.

Keywords—*painting classification; image dataset; CNN*

I. INTRODUCTION AND BACKGROUND

Due to the substantial digitization of artworks in recent years, along with the impressive development in the area of computer vision, automated painting classification is an interesting and crucial research problem. Fine-art painting classification, which includes identifying the artist and the artistic style from a painting, has many applications in museums, various industries, painting theft investigation, forgery detection, art education, etc. However, this is not a trivial task due to the complexities of artistic styles, subjectivity in the interpretation of paintings, varied image quality, lack of fine details, and context of the visual images [1] [2].

In the last decade, several studies have focused on employing computer vision techniques to analyze paintings and other forms of visual art [3]–[6]. In our previous work [7], we explored the use of pre-trained Convolutional Neural Network (CNN) models as a feature extraction tool for painting classification. Some of the popular painting datasets that are available publicly for artist and style classification include the Painting-91 dataset by [8], the WikiArt dataset [9], and the

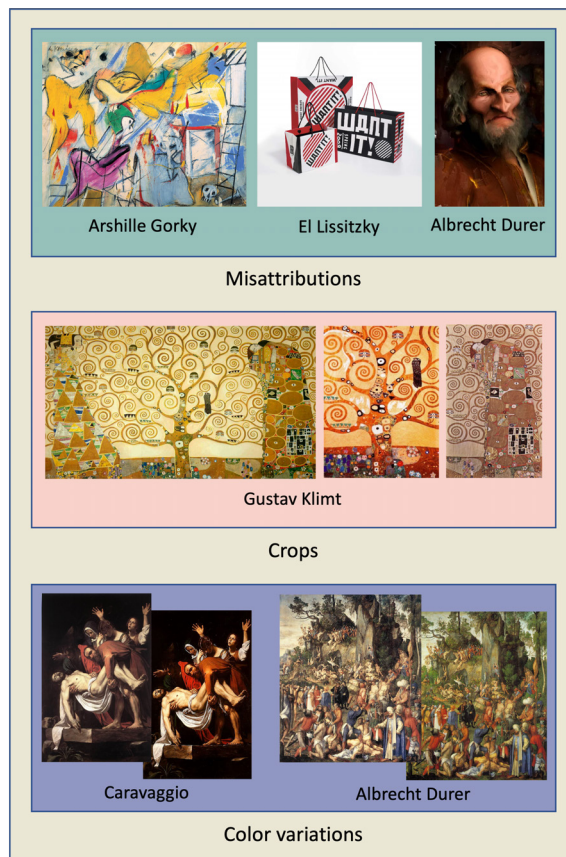


Figure 1. Some errors that exist in the old Painting-91 dataset.

Painting dataset consisting of ten classes of fine-art paintings from the PASCAL VOC [10].

While CNNs have proven to be versatile and effective in various image-related tasks, one of the major challenges of being able to effectively use CNNs for painting classification is the need for large hand-labeled datasets [2]. To that end, in this paper, we have worked on improving the existing Painting-91 dataset [8] to not only include newer artists and painting styles, but also carefully remove different mis-attribution and other human errors that existed in that dataset. Some of these errors are shown in Figure 1. Our newly constructed dataset, called the Paintings-100 dataset, also has enhanced image resolutions than the previous dataset. We have augmented certain artist categories, which had fewer images in the previous dataset,



Figure 2. Some paintings of the newly added nine artists that are included in the Paintings-100 dataset.

with newer images. Last, but not the least, we have also done a preliminary evaluation of this dataset using several CNN based methods on both whole images as well as random image patches for the artist classification task.

The rest of this paper is organized as follows. Section II and its subsections outline in detail the dataset constructed in this work. The techniques used to evaluate the classification performance on this dataset, the experiments performed, and results obtained are described in detail in Section III. Finally, we list our conclusions and directions for future research in Section IV.

II. DATASET CONSTRUCTION

When we worked on [7], we realized that the images in the original Painting-91 dataset [8] are too small for learning meaningful features using deep learning. While trying to replace the images with their high-resolution versions, we found several kinds of human errors and other limitations in the original dataset which needed to be fixed. These issues, some of which are shown in Figure 1, are as follows:

A. Low resolution

This was the main motivation for this work. The mean size of an image in this dataset is 268×263 pixels. These dimensions are smaller than the input sizes of many CNN models. So, to improve the quality of the data, we started replacing the images with high-resolution versions downloaded from the Internet via Google Reverse Image Search [11]. We were successful in this task for about 97% of the images, but we also ran into other errors as detailed next.

B. Mis-attributions

These are images labeled with a painter’s name that are not painted by that painter. Some of these mis-attributed images are deliberate attempts to copy the attributed painter’s style, some are created using image editing software by making collages of existing paintings, and some others have simply

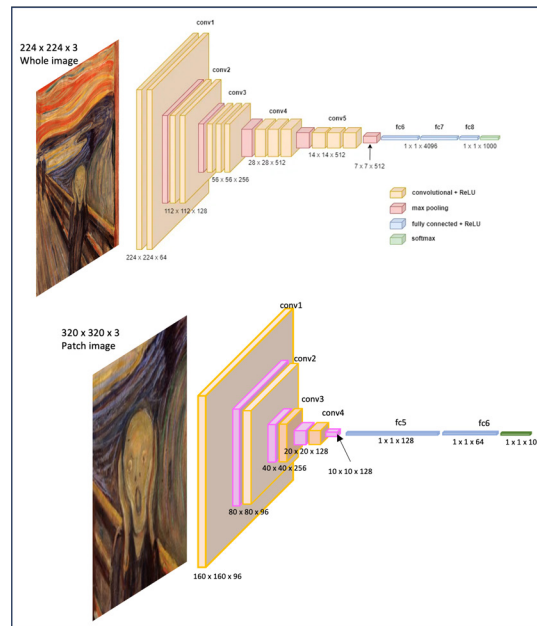


Figure 3. For artist classification task, we used both whole images as well as random patches from the images to feed into different CNN models.

been downloaded from a source on the Internet which also had the wrong label.

C. Duplicates

Several of the images in most artist classes are duplicates of other images also in the class. The number of images per class varies from 30 to 51, which is already very small for training deep learning models, and the presence of duplicate and mislabeled images further reduces this number. For instance, the painter class Hieronymus Bosch has 50 paintings, out of which 25 are duplicates (exact or slightly variant copies), and a further 5 are wrongly attributed, thus bringing the actual number of usable images down to 20.

D. Cropped images

These are images which show only part of a painting, the whole of which may or may not be present in the dataset. Since the overall composition bears as much information about

TABLE I
NEW ARTISTS WHOSE PAINTINGS WERE ADDED TO THE DATASET, ALONG WITH THEIR NATIONALITY AND STYLE.

Artist	Nationality	Style
Amrita Sher-Gil	Hungarian-Indian	Several
Jamini Roy	Indian	Indian folk art
Julie Mehretu	Ethiopian American	Several
Katsushika Hokusai	Japanese	Ukiyo-e
Kitagawa Utamaro	Japanese	Ukiyo-e
Rafiy Okefolahan	Cape Verdean	Contemporary multimedia
Raja Ravi Varma	Indian	Indian realism
Utagawa Hiroshige	Japanese	Ukiyo-e
Zhang Xiaogang	Chinese	Surrealism

a painter’s identity as details do, just having a small cropped portion of a painting in the dataset is not ideal.

E. Color variations

These are also copies of other images in the dataset. However, instead of being exact duplicates, these images have a different color palette. There is no way of knowing which of the copies has a more accurate color palette, and so, color cues lose their significance in classification. To further complicate matters, some artists (such as Andy Warhol) themselves produced multiple copies of the same painting with slight differences in details and color, which count as different images in the dataset.

F. Lack of diversity

While the original dataset contains an impressive collection of works from 91 painters and 13 style categories, this collection focuses exclusively on Europe and the Americas. There are no painters representing the rich artistic heritage of Asia and Africa. This is not exactly an error, but an omission in the dataset that needed to be addressed for overall improvement.

Improvements

We took several steps to address the above issues. First, we replaced most images with their high-resolution versions wherever such a version was available in the public domain. The mean image size in the new dataset is $1,523 \times 1,493$ pixels. This amounts to a 32-fold increase in the number of pixels per image, on average. Second, we replaced wrongly labeled images with their correct counterparts, or new images by the same artist. Third, wherever possible, we also added new paintings to all artist categories that had less than 50 paintings. Fourth, we reduced the number of duplicates by replacing them with new paintings wherever possible. Last, but not the least, we added 50 paintings each by 9 more painters spanning a diverse array of styles representing Asian and African art (shown in Figure 2 and Table I). This makes our new Paintings-100 dataset a more diverse, inclusive and representative database of fine-art paintings. The presented Paintings-100 dataset has 5,357 images which is an impressive 25% increase from the 4,266 image Painting-91 dataset.

III. EXPERIMENTS AND DISCUSSION

The original Painting-91 dataset, and by extension, the proposed Paintings-100 dataset, are both designed for two classification tasks. These tasks are artist classification and style classification. The first task is straightforward as every image has an artist class label, and the artist classes are roughly equal in size. For the second task, the dataset contains 14 style class labels in addition to the 100 artist class labels. This is a slight increase from 13 style classes in the Painting-91 dataset (Ukiyo-e is the new style class introduced). Each style class contains works from more than one artist, but not all artists have a style class label [8]. In the current work, we have only analyzed the dataset with respect to the first problem.

The artist classification problem is somewhat challenging for CNN-based models. This is mainly due to two reasons.

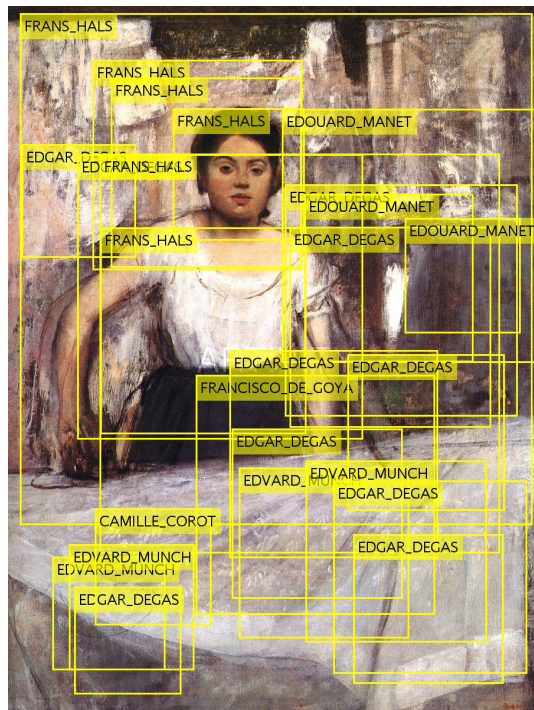


Figure 4. Painting by Edgar Degas. When the whole image is used for artist recognition, the CNN identified it as a Frans Hals painting, whereas by using random patches, it is correctly classified as an Edgar Degas artwork.

Firstly, deep learning is data-hungry, and very few artists manage to paint more than a few dozen completed paintings in their lifetime. This severely reduces the images available for training. Secondly, CNN models take fairly low-resolution images as their input. This means, we either need to down-sample the images and lose all detail, or crop the images and lose all sense of composition and context. Since neither solution was fully acceptable to us, we decided to use an ensemble of multiple CNN models that use both downsampled whole images and full-size patches cropped out of the high-resolution images. For classifying the patches, we designed our own CNN from scratch and trained it using 25 random square patches from each training image. For the whole image classification, we fine-tuned the VGG-16 network [12] trained on the ImageNet image dataset [13]. These two models are shown in Figure 3. In both cases, we used 24 images per class with augmentation for training, 6 per class for validation, and the rest for testing. We used decision fusing based on the labels predicted by the two models. Our initial results were promising, with the patch-based model yielding a 32% accuracy on the test set, the whole image model yielding 33%, and the fused accuracy at 38%. The confusion matrix for this result is shown in Figure 5. Figure 4 illustrates the effectiveness of such a fusion. In this example, although the whole image classifier predicts the label to be Frans Hals, different patches vote for different labels and the true artist, Edgar Degas, gets the most votes.

We also did a visualization of the responses from the

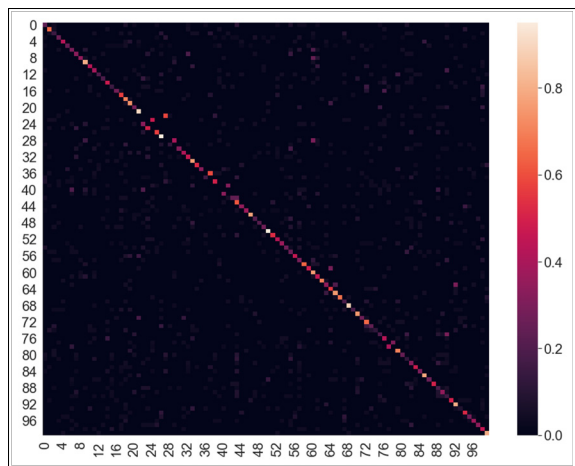


Figure 5. The confusion matrix for the artist classification experiment using the combined decision of two CNN models. The rows indicate actual class index values while the columns indicate predicted index values.

last convolutional layer of our patch-image classifying CNN using the Grad-CAM technique [14]. This "heatmap" analysis highlights the regions of an image that are key identifiers for artist recognition. While this is a work in progress, the results demonstrated in Figure 6 show some of the characteristics of artists that the network can identify correctly. For instance, bold outlines are a signature characteristic of Jamini Roy and these outlines are highlighted in the topmost example in Figure 6. Similarly, dotted patterns and certain kinds of brush strokes are recognized as characteristic features of Roy Lichtenstein and Vincent Van Gogh, respectively.

IV. CONCLUSION AND FUTURE WORK

In this work, we presented a large scale diverse high-resolution image dataset for artist and style classification. While this was based on the Painting-91 dataset, the improvements were significant enough for the Paintings-100 dataset to be considered a new dataset. Although we need to run many more experiments, initial results based on an ensemble of CNN models showed promising results for the artist classification task.

There are many different ideas that we would like to try out on this dataset in the near future. Currently, we select the patches randomly. In future, we want to try selecting patches with face detectors and object detectors to see how that affects our results. We plan to use some color normalization techniques to reduce the effect of photographic conditions on the paintings. Last, but not the least, we still need to run style classification experiments on this dataset and see the results.

REFERENCES

[1] J. M. Silva, D. Pratas, R. Antunes, S. Matos, and A. J. Pinho, "Automatic analysis of artistic paintings using information-based measures," *Pattern Recognition*, vol. 114, 2021, p. 107864.

[2] E. Cetinic, T. Lipic, and S. Grgic, "Fine-tuning convolutional neural networks for fine art classification," *Expert Systems with Applications*, vol. 114, 2018, pp. 107–118.

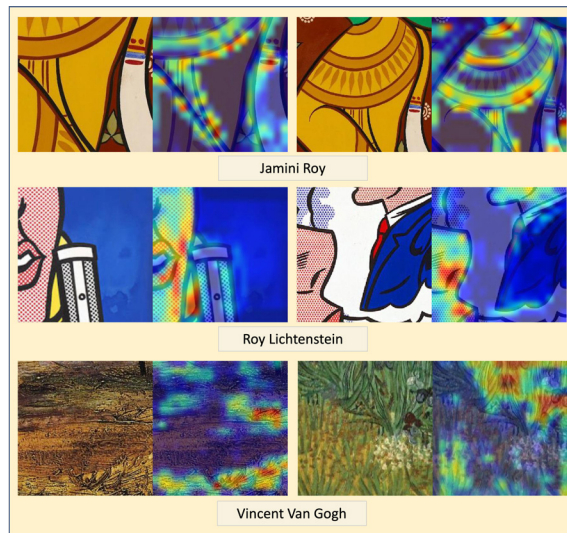


Figure 6. Some paintings and their heatmaps showing regions of interest for artist recognition as detected by the CNNs.

[3] R. S. Arora and A. Elgammal, "Towards automated classification of fine-art painting style: A comparative study," in *Proceedings of the 21st International Conference on Pattern Recognition (ICPR2012)*, 2012, pp. 3541–3544.

[4] C. S. Rodriguez, M. Lech, and E. Pirogova, "Classification of style in fine-art paintings using transfer learning and weighted image patches," in *2018 12th International Conference on Signal Processing and Communication Systems (ICSPCS)*, 2018, pp. 1–7.

[5] S. Smirnov and A. Eguizabal, "Deep learning for object detection in fine-art paintings," in *2018 Metrology for Archaeology and Cultural Heritage (MetroArchaeo)*, 2018, pp. 45–49.

[6] C. Sandoval, E. Pirogova, and M. Lech, "Two-stage deep learning approach to the classification of fine-art paintings," *IEEE Access*, vol. 7, 2019, pp. 41 770–41 781.

[7] S. Banerji and A. Sinha, "Painting classification using a pre-trained convolutional neural network," in *Proceedings of the 2nd Workshop on Computer Vision Applications (WCVA) at the Tenth Indian Conference on Vision, Graphics and Image Processing (ICVGIP)*, 2016, pp. 168–179.

[8] F. S. Khan, S. Beigpour, J. V. de Weijer, and M. Felsberg, "Painting-91: A large scale database for computational painting categorization," *Machine and Vision Application (MVAP)*, vol. 25, no. 6, 2014, pp. 1385–1397.

[9] B. Saleh and A. Elgammal, "Large-scale classification of fine-art paintings: Learning the right metric on the right feature," *International Journal for Digital Art History*, no. 2, Oct. 2016, pp. 70–93.

[10] E. J. Crowley and A. Zisserman, "In search of art," in *Workshop on Computer Vision for Art Analysis, ECCV*, 2015, pp. 54–70.

[11] "Google reverse image search," <https://www.google.com/imghp>, accessed: December 29, 2023.

[12] K. Simonyan and A. Zisserman, "Very deep convolutional networks for large-scale image recognition," in *3rd International Conference on Learning Representations, ICLR 2015, San Diego, CA, USA, May 7-9, 2015, Conference Track Proceedings*, 2015.

[13] J. Deng et al., "Imagenet: A large-scale hierarchical image database," in *2009 IEEE Conference on Computer Vision and Pattern Recognition*, 2009, pp. 248–255.

[14] R. R. Selvaraju et al., "Grad-cam: Visual explanations from deep networks via gradient-based localization," in *2017 IEEE International Conference on Computer Vision (ICCV)*, 2017, pp. 618–626.

Evaluation of Multi-Angle System for Reflecting Piano Lessons

Md Saidi Muhammad Ashraf Naim, Naoki Morita
 School of Information Telecommunication Engineering
 Tokai University
 Tokyo, Japan
 e-mail: {0cjt2118@cc, wv062303@tsc}.u-tokai.ac.jp

Kenta Morita
 Faculty of Medical Engineering Dept.
 Suzuka University of Medical Science
 Mie, Japan
 e-mail: morita@suzuka-u.ac.jp

Chiharu Nakanishi, Chiaki Sawada
 Kunitachi College of Music
 Tokyo, Japan
 e-mail: {nakanishi.chiharu, sawada.chiaki}@kunitachi.ac.jp

Kazue Kawai
 Faculty of Literature
 Seitoku University
 Chiba, Japan
 e-mail: kawai.kazue@wa.seitoku.ac.jp

Abstract—The author aims to pass on the tradition of classical music to the next generation by significantly reforming and evolving the traditional pedagogy of piano education. Recording and reflecting on one’s performance through video can be a helpful tool in the learning process. However, current video platforms lack the functionality to quickly cue specific scenes. Moreover, video recording is generally limited to a single angle. Reflecting on not just the hands but also the use of the upper body and feet is crucial in piano performance. We have developed a system that enables multi-angle recording using multiple smartphones, allowing for the review of video linked to the musical score. This paper will discuss the system’s development, focusing on the synchronization between audio and every video angle, and user reviews. Utilizing this system for objective evaluation of actual performances is expected to reveal gaps between the ideal and reality and to discover new challenges.

Keywords—Piano Lesson; support; Multi-Angle recording system; visualization.

I. INTRODUCTION

This paper is part of a research project conducted at a music university in Japan, aimed at passing down the tradition of classical piano to the next generation. Previous piano studies [1] - [4] have primarily focused on beginners, aiming to record and analyze performance techniques, such as pointing out errors and playing habits. While multi-angle video recording can be achieved using multiple cameras, reviewing these recordings simultaneously requires aggregating data and editing with specialized software, making instant post-performance review challenging. Our study targets music university students, with a focus on lessons for acquiring musical expression. To master musical expression, repeated practice is necessary to understand the nuances in sound created by different playing styles. Therefore, it’s crucial to instantly review one’s playing technique and the resulting sound. We are developing a system that utilizes smartphones and tablets for recording performances from multiple angles. This system allows for

immediate playback from specific annotated points [5], enabling performers to promptly reflect on their technique.

The remainder of this paper is organized as follows. Section II describes the multi-angle recording system being developed in this study, and Section III describes the results of two experiments. Finally, Section IV presents the conclusions and future challenges of this research.

II. SYNCHRONIZED RECORDING SYSTEM USING MULTIPLE SMARTPHONES

The architecture of our system is composed of a server-client model. On the server side, the system is implemented using the Laravel framework, while on the client side, it is developed using Vue.js. This system has been tested for operation using Chrome browsers on PCs, iOS, and Android.

A. Recording

This section describes a multi-angle recording method using three perspectives: upper body, hands, and feet, utilizing four smartphones. One smartphone is logged into the system and serves as the controller for starting and stopping recordings and capturing audio. The other smartphones are used as video cameras. Recording is synchronized with the start/stop signal from the controller device, and automatically uploaded to the server upon completion. Adding camera angles is streamlined by scanning a QR code displayed by the controller machine, which transfers user information and automatically directs to the recording standby page. The system’s design allows for the addition of angles corresponding to the number of smartphones prepared. If only one smartphone is available, it can be utilized by turning on the video function on the controller device.

B. Reflection

When the user clicks on an index (score name and practice time) on the calendar, the score and the video are displayed. Figure 1 is the viewing page. One angle of the video is displayed prominently, while the remaining angles

are displayed as thumbnails. Selecting a thumbnail switches between the enlarged display and the thumbnail display. During playback, the audio comes from the microphone recorded by the controller device, and the video displays all angles simultaneously. In the example in Figure 1, annotations are added at two different measures during the initial listening session. These annotations are also useful for reflecting simultaneously from the second time onward.

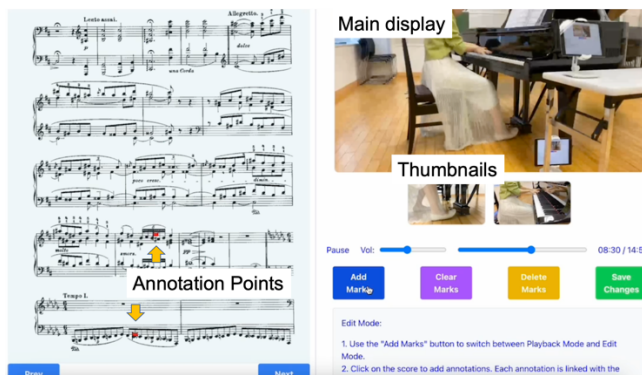


Figure 1. Example of score and video viewing page.

III. SYSTEM EVALUATION

A. Difference in video timestamps

The system compiles video from each device onto a server after recording ends, making it accessible to users instantly. The audio captured by the microphone was compared with the audio from three video recordings, which were not utilized during the reflection phase. The results revealed a discrepancy ranging from 0.03 to 0.29 seconds. This is the timing discrepancy between each device receiving the recording start signal from the controller and the actual commencement of recording.

B. User Reviews

Interviews were conducted with four students and one teacher to gather feedback on the system.

1) *Audio Discrepancy*: A notable discrepancy in audio timing, 0.29 seconds as reported by a student caused discomfort, though some students found it negligible. The teacher deemed a discrepancy as minimal as 0.03 seconds to be intolerable for educational use, emphasizing that precision within 0.01 seconds is fatal.

2) *Multi-Angle Recording*: Students noted its benefit for observing their full body and foot movements, which are typically not visible when only focusing on hand movements. Reviewing each angle's video separately is not practical. Having the capability to simultaneously reflect on multiple angles in a single view is highly convenient. However, the teacher highlighted the inadequacy of video for detailed foot technique analysis, noting that even with this system or standard iPhone recording, audio-video discrepancies can emerge. Specifically, the delayed auditory feedback from pedal use, as opposed to the immediate

response from hand movements, underscores the necessity for improved visualization of pedal pressure and timing in such recordings.

3) *Annotation Feedback*: Users highly appreciated the feature for swiftly returning to annotated sections in lengthy pieces. Despite the initial effort to annotate these points, the ease of revisiting them was noted as a major benefit.

4) *Suggestions for Improvement*: The students suggested adding a 10-second rewind and fast-forward feature. They highlighted the need for easier navigation through small sections of the video, finding the current method of using the progress bar for minor adjustments to be less efficient and user-friendly.

IV. CONCLUSION AND FUTURE WORK

In this study, we aimed to record piano performances in multi-angles to enable performers to check their body movements. A multi-angle recording system was developed, utilizing multiple smartphones working in tandem. The results showed that the system was effective for student self-review. However, for professional levels, like teachers, it was evident that the system requires further improvement.

Future tasks include addressing three main points: First, not only synchronizing the start of the recordings but also adjusting the playback timing of each file to eliminate discrepancies between audio and video. Second, beyond reviewing from annotated points, a feature for instant access to desired timestamps, like 10-second skips, is necessary. Third, for foot pedal usage, it was discovered that video of that angle alone is insufficient, and visualization of the force and extent of pedal engagement is required.

ACKNOWLEDGMENT

The present study was supported by the Japan Society for the Promotion of Science (JSPS) through KAKENHI Grant Number 21K18528.

REFERENCES

- [1] K. Ueda, Y. Takegawa, and K. Hirata, "Design and Implementation of a Piano Learning Support System Focusing on Visualization of Keying Information and Annotation," *IPSJ Journal*, Vol. 57, No. 12, pp.2617-2025, 2016.
- [2] T. Suzuki, K. Tanaka, R. Ogura, and Y. Tsuji, "Practice of Beginners' Piano Skill Training Support Using 'Visualization System for Piano Performance (VSPP)'," *IPSJ SIG Technical Report*, Vol.2018-MUS-119 No.16, pp.1-6, 2018.
- [3] R. Matsui, Y. Takegawa, and K. Hirata, "Tel-Gerich: Remote Piano Lesson System Considering Joint Attention Camera Switching and Camera Switching," *Human interface: the transaction of Human Interface Society*, Vol.20, No.3, pp.321-332, 2018.
- [4] R. Matsui, A. Hasegawa, Y. Takegawa, K. Hirata, and Y. Yanagawa, "Design, Implementation and Assessment of a Support System to Find Bad Fingering Habits for Piano Teachers," *IPSJ Journal*, Vol. 61, No. 4, pp.789-797, 2020.
- [5] N. Morita, et al., "Synchronized Recording System Using Multiple Smartphones," *Proceedings of SOCIETY TRENDS 2023*, pp.12-14, 2023.

Key Ideas in Parameter Estimation

Pavel Loskot
 ZJU-UIUC Institute
 Haining, China

e-mail: pavellok@intl.zju.edu.cn

Abstract—Parameter estimation plays a crucial role in many applications of statistical signal processing. Estimation theory is a well-established and rigorous framework for making the statistical inferences from noisy observations. It yields the best possible (in a precisely defined sense), interpretable and numerically effective procedures, provided that the models of measurements and of signals are known up to unknown parameters. Understanding the fundamental principles of parameter estimation is nowadays also important in designing the interpretable machine learning architectures, which usually exchange the computational complexity for the superior performance, while alleviating the need for knowing the models of signals and measurements. This paper comprehensively outlines the key principles of estimating the time-invariant random and non-random parameters, which are accompanied by several illustrative examples. The presentation focuses on the key ideas, and does not cover many other relevant topics; for example, neither the estimation of time-varying signals nor the survey of the research literature are considered.

Keywords—Inference; linear estimator; noise; optimum estimator; parameter estimation; risk function; uncertainty.

I. INTRODUCTION

The common task in many applications of statistical signal processing is to learn the values of hidden parameters, and to extract other useful information from noisy measurements. This must be done statistically, i.e., the good-quality parameter estimates must be obtained with a high probability, i.e., most of the time. As illustrated in Figure 1, the unknown values of parameters are mapped to measured signals, which are distorted by the measurement noise. The goal is to find the optimum mapping for the measurements in order to recover the parameter values of interest with as small error as possible, despite the presence of other nuisance parameters and the measurement noise. Since the mapping of parameters to measurements is assumed to be known, one might be tempted to simply undo the mapping by using the corresponding inverse mapping. This may be a simple strategy for estimating the parameter values, provided that the inverse mapping can be obtained. However, the caveat is that the inverse mapping usually amplifies the measurement noise, so it is only effective if the noise is sufficiently small, and thus, can be neglected. In practice, this is often not the case, and more sophisticated methods of the parameter estimation are required.

The best possible target mapping representing the estimator is usually formulated as the solution of a constrained or unconstrained optimization problem. The optimization problem is defined, so that the estimation error is minimized in some sense. This is also dependent on how the estimated values are used in a given signal processing application. However,

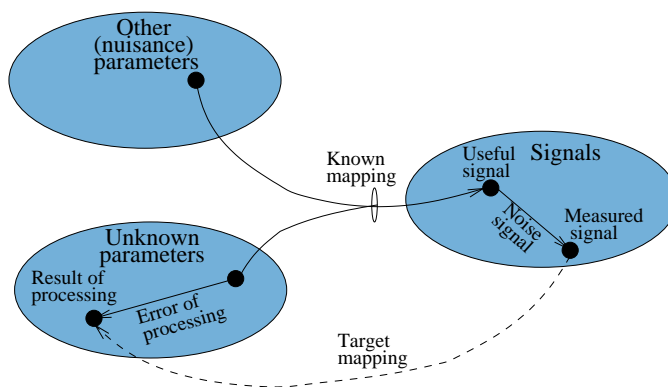


Figure 1. The mapping of parameters to measured signals, and the inverse mapping of measurements to the estimated parameter values.

the resulting optimization problem may not have any solution, for example, since some important knowledge is missing, or it may be too complex to be solved effectively. In such a case, the estimator can be constrained to be a linear filter. This greatly limits the implementation complexity, although the optimality can now be only considered within the class of linear filters. The solution of the optimization problem can be sometimes found analytically in a closed-form, otherwise it must be obtained numerically.

The solution of the optimization problem answers one of the following two questions, depending on the application, i.e.:

- 1) “Which from several defined values the parameter has?”
- 2) “How big is the parameter value?”

The first question is central in detection theory, and it is also closely related to the optimum decision and the hypothesis testing problems. The second question is the subject of this tutorial, i.e., it defines the point estimates of the parameter within estimation theory. The parameter estimates can be also obtained as ranges of values, however, the interval estimates are not considered in this tutorial.

If the parameters vary in time, they are referred to as signals in engineering applications of statistical signal processing. In mathematics, the term, process, instead of signal is usually preferred, and the parameter estimation is studied as one of the tasks of statistical inference. In data science, the longitudinal data in discrete time are referred to as sequences or time-series, and the estimation problems are referred to as data mining.

In general, there are three levels of statistics that can be obtained for the measurements as indicated in Figure 2. In par-

ticular, the parametric and non-parametric descriptive statistics are used in characterizing and summarizing the measurements in observational studies. In order to estimate the values of hidden parameters, which cannot be observed directly, the inferential statistics require using more sophisticated methods as discussed above. Finally, the causal inferences are used to determine, for example, the counterfactual outcomes and other cause-effect relationships, which is, however, beyond the scope of this tutorial.

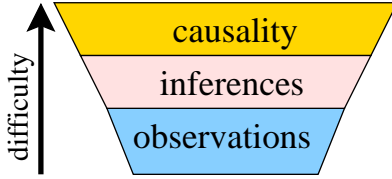


Figure 2. The three levels of statistically processing the measurements.

A random signal at any particular time instant is a random variable. The processing of continuous time signals can exploit derivatives, whereas differences are used for signals in discrete time (the time discretization does not automatically replace derivatives with differences). The important consideration in estimating the parameter values is whether their prior probability distribution is known; in such a case, the parameters can be considered to be random, and the Bayesian inference methods are used. Otherwise, without any prior knowledge, the unknown parameters must be treated as being non-random (i.e., deterministic). There are, however, many situations when some prior parameter statistics are known (e.g., the mean and the variance), or their probability distribution is known partially; these cases must be considered individually as they do not constitute the case of random nor non-random parameters.

There are generally four basic types of the parameter estimation problems depending whether the prior probability distribution of the parameter to be estimated is known or not, and whether the estimator is general (i.e., unconstrained), or it is a linear filter or a transformation.

The rest of this tutorial is organized as follows. The problem of finding the best possible estimator for a random parameter minimizing so-called risk function is outlined in Section II. It includes the Minimum Mean-Square Error (MMSE) and the Maximum a Posteriori (MAP) estimators. If the prior distribution of the parameter is not known, it must be treated as being non-random as explained in Section III. This case includes the Minimum Variance Unbiased (MVUB), the Maximum Likelihood (ML), the Least Squares (LS) and the moment-based estimators. For these estimators, the Cramer-Rao Lower Bound (CRLB) of their performance has been defined. Linear estimators of random and non-random parameters are considered in Section IV and Section V, respectively. Additional solved problems are provided in Section VI. The relevant textbooks and the topics and problems, which are not covered in this tutorial are summarized and discussed in Section VII. Finally, Section VIII concludes the paper.

II. GENERAL ESTIMATION OF RANDOM PARAMETERS

Consider first the case of a general estimation of a continuous or discrete random parameter, P , having the known prior Probability Density Function (PDF), $f_P(p)$, or the Probability Mass Function (PMF), $\Pr_P(p)$, respectively. The parameter P is observed as the value (or multiple values), $X(P)$, representing the system being considered, i.e., it is crucial that the dependence of X on P is known. It is then possible to derive the statistical dependence of X on P represented by the conditional density, $f_{X|P}(x|p)$, or the conditional probability, $\Pr_{X|P}(x|p)$, respectively. The estimator converts the measurements, $X(P)$, to the parameter estimates, $\hat{P}(X)$, which are used in a given application. The application dictates how to define the estimation errors, $\mu(\hat{P}(X), P)$. The overall process is summarized in Figure 3.

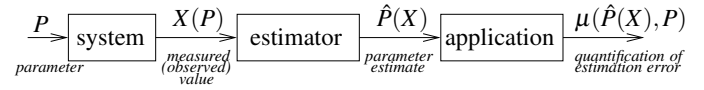


Figure 3. A formulation of the parameter estimation problem.

Since the parameter, P , is assumed to be random, the function, $\mu(\hat{P}, P)$, quantifying the estimation error, $(\hat{P} - P)$, is a random variable. In order to minimize the estimation error for any value of P (which is unknown), the optimum estimator minimizes the mean value, or so-called the risk, $E[\mu(\hat{P}, P)]$, where $E[\cdot]$ denotes expectation. For instance, the MMSE estimator minimizes the risk, $E_{X,P}[\mu(\hat{P}(X), P)] = E_{X,P}[(\hat{P}(X) - P)^2]$, whereas the probability that the error is greater than a threshold, Δ , assumes the risk function, $E_{X,P}[\mu(\hat{P}(X), P)] = \Pr(|\hat{P}(X) - P| > \Delta)$, as illustrated in Figure 4.

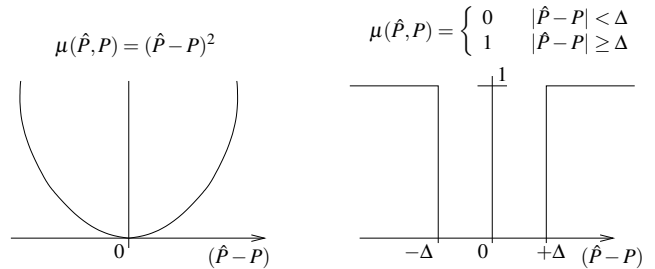


Figure 4. The two examples of risk function for designing estimator, $\hat{P}(X)$.

In particular, the optimum estimator of a random parameter, P , minimizes the general risk function,

$$E_{X,P}[\mu(\hat{P}(X), P)] = \int_{\{X\}} \int_{\{P\}} \mu(\hat{P}(x), p) f_{X,P}(x, p) dp dx. \quad (1)$$

The risk (1) is minimized, if and only if,

$$\hat{P}_{\text{opt}} = \operatorname{argmin}_{\hat{P}(x)} E_{X,P}[\mu(\hat{P}(x), P) | X = x]. \quad (2)$$

Remark 1. The expressions presented here assume that P and X are scalar random variables; the extension to random vectors is (usually) straightforward.

A. The MMSE Estimator

Substituting the MMSE function, $\mu(\hat{P}, P) = (\hat{P} - P)^2$, into (1) above, the MMSE estimator is defined as,

$$\begin{aligned} \hat{R}_{\text{MMSE}}(x) &= E_P[P|X = x] = \int_{\{P\}} p f_{P|X}(p|x) dp \\ &= \frac{\int_{\{P\}} p f_{X,P}(x,p) dp}{f_X(x)} = \frac{\int_{\{P\}} p f_{X|P}(x|p) f_P(p) dp}{\int_{\{P\}} f_{X|P}(x|p) f_P(p) dp}. \end{aligned} \quad (3)$$

Hence, if no measurements are available at all, the optimum MMSE estimator is, $\hat{R}_{\text{MMSE}} = E_P[P] = \bar{P}$ (the mean of P).

Example 1. The signal samples, $x(i)$, $i = 1, 2, \dots, n$ represent the sum of a random, but otherwise constant parameter, P , having the uniform PDF over the interval, $(0, d)$, and a zero-mean stationary white Gaussian noise, $w(i)$, having the known variance, σ_w^2 . The noise samples, $w(i)$, and the parameter, P , are independent. Find the MMSE estimate of P .

Solution: 1. For $P = p$, the measured signal, $x(i) = p + w(i)$, has the conditional PDF,

$$\begin{aligned} f_{X|P}(x|p) &= \prod_{i=1}^n f_w(x(i) - p) \\ &= \frac{1}{\sqrt{(2\pi\sigma_w^2)^n}} \exp\left(-\frac{1}{2\sigma_w^2} \sum_{i=1}^n (x(i) - p)^2\right). \end{aligned} \quad (4)$$

The prior PDF of the parameter, $f_P(p) = \frac{1}{d}$, for $p \in (0, d)$, and 0, otherwise. Thus, the PDF of X is,

$$\begin{aligned} f_X(x) &= \int_{-\infty}^{\infty} f_{X|P}(x|p) f_P(p) dp = \frac{1}{d} \int_0^d \prod_{i=1}^n f_w(x(i) - p) dp \\ &= C_n \exp\left(-\frac{1}{2\sigma_w^2} \left(n\bar{x}^2 - \sum_{i=1}^n x^2(i)\right)\right) \times \\ &\quad \times \left(Q\left(-\frac{\bar{x}}{\sigma_w} \sqrt{n}\right) - Q\left(\frac{d-\bar{x}}{\sigma_w} \sqrt{n}\right)\right) \end{aligned} \quad (5)$$

where $C_n = (d\sqrt{n})^{-1} (2\pi\sigma_w^2)^{-(n-1)/2}$, $Q(u) = \int_u^{\infty} \frac{1}{\sqrt{2\pi}} e^{-t^2/2} dt$ (the Q-function), and, $\bar{x} = \frac{1}{n} \sum_{i=1}^n x(i)$, so the MMSE estimator,

$$\begin{aligned} \hat{R}_{\text{MMSE}}(n) &= \int_{-\infty}^{\infty} p f_{P|X}(p|x) dp \\ &= \bar{x} - \frac{\sigma_w}{\sqrt{n}} \frac{Q\left(-\frac{\bar{x}}{\sigma_w} \sqrt{n}\right) - Q\left(\frac{d-\bar{x}}{\sigma_w} \sqrt{n}\right)}{Q\left(-\frac{\bar{x}}{\sigma_w} \sqrt{n}\right) - Q\left(\frac{d-\bar{x}}{\sigma_w} \sqrt{n}\right)} \triangleq g(\bar{x}, n). \end{aligned} \quad (6)$$

For streaming data, the online MMSE estimator is obtained assuming a recurrent evaluation of the arithmetic average, i.e.,

$$\bar{x} = \frac{1}{n} \sum_{i=1}^n x(i) = \frac{x(n)}{n} + \frac{n-1}{n} \underbrace{\frac{1}{n-1} \sum_{i=1}^{n-1} x(i)}_{\bar{x}(n-1)}. \quad (7)$$

The corresponding circuit is shown in Figure 5. ■

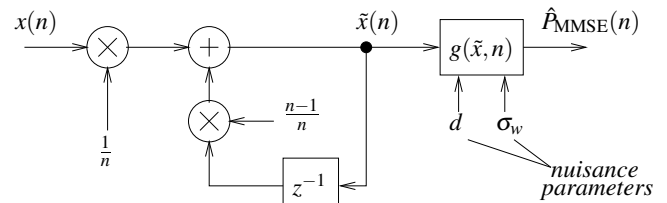


Figure 5. The MMSE estimator for streaming data from Example 1.

The nuisance parameters that appeared in Figure 1 and Figure 5 are the parameters that affect the measured signal, however, they are otherwise irrelevant in the application considered. Consequently, the nuisance parameters can be estimated, and these estimates simply ignored. Alternatively, the estimated nuisance parameters can be substituted into the estimator of the parameters of interest; this method is referred to as an adaptive estimation. The third strategy often used in practice is to eliminate the random nuisance parameters, N , from the distribution of the measurements, $X(P, N)$, i.e.,

$$\hat{R}_{\text{MMSE}} = \int_{\{P\}} p \underbrace{\int_{\{N\}} f_{P,N|X}(p, n|X = x) dn}_{f_{P|X}(p|X=x)} dp = E_P[P|X = x]. \quad (8)$$

The average MMSE estimator (8) is then considered to be good enough, for any specific values of N .

Omitting the derivations and proofs, the MMSE estimates have the following properties.

- The estimation error of the MMSE estimator has zero-mean, i.e., the MMSE estimates are unbiased:

$$E[\hat{R}_{\text{MMSE}}(X) - P] = 0 \Rightarrow E[\hat{R}_{\text{MMSE}}(X)] = E[P]. \quad (9)$$

- The estimator variance can be expressed as,

$$\begin{aligned} \text{var}[\hat{R}_{\text{MMSE}} - P] &= E\left[\left((\hat{R}_{\text{MMSE}} - P) - E[(\hat{R}_{\text{MMSE}} - P)]\right)^2\right] \\ &= \text{var}[P] - \text{var}[\hat{R}_{\text{MMSE}}]. \end{aligned} \quad (10)$$

- The estimation error is uncorrelated with (i.e., orthogonal to) an arbitrary function of X , i.e.,

$$\begin{aligned} \text{cov}[\hat{R}_{\text{MMSE}}(X), g(X)] &= \text{cov}[P, g(X)] \\ &= E[\hat{R}_{\text{MMSE}}(X)g(X)] - \underbrace{E[\hat{R}_{\text{MMSE}}(X)]}_{E[P]} E[g(X)]. \end{aligned} \quad (11)$$

Consequently, $\text{cov}[\hat{R}_{\text{MMSE}} - P, g(X)] = 0$, and for $g(X) = \hat{R}_{\text{MMSE}}(X)$,

$$\text{cov}[\hat{R}_{\text{MMSE}} - P, \hat{R}_{\text{MMSE}}] = 0. \quad (12)$$

Remark 2. The unbiased estimator does not suffer from a systematic error. Moreover, the estimator quality is generally quantified as the variance of its estimation error.

Theorem 1 (Gauss-Markov theorem). Let \mathbf{P} and \mathbf{X} be the vector of parameters to be estimated, and the vector of measurements, respectively. If \mathbf{P} and \mathbf{X} are jointly Gaussian,

i.e., \mathbf{P} and \mathbf{X} are Gaussian with the means, $\bar{\mathbf{P}}$, and, $\bar{\mathbf{X}}$, and the covariance matrices, $\text{var}[\mathbf{P}]$, and, $\text{var}[\mathbf{X}]$, respectively, then,

$$\hat{\mathbf{P}}_{\text{MMSE}}(\mathbf{x}) = \bar{\mathbf{P}} + \mathbf{H}(\mathbf{x} - \bar{\mathbf{X}}), \quad \mathbf{H} = \text{cov}[\mathbf{P}, \mathbf{X}] \text{var}^{-1}[\mathbf{X}]. \quad (13)$$

The covariance matrix of the estimation error is,

$$\text{var}[\hat{\mathbf{P}}_{\text{MMSE}} - \mathbf{P}] = \text{var}[\mathbf{P}] - \text{cov}[\mathbf{P}, \mathbf{X}] \text{var}^{-1}[\mathbf{X}] \text{cov}[\mathbf{X}, \mathbf{P}]. \quad (14)$$

Example 2. Let, $x(t) = A + w(t)$, be an observed signal over the time interval, $t \in (0, T)$, where A is a normally distributed random variable with known mean, \bar{A} , and known variance, σ_A^2 , and $w(t)$ represents a zero-mean Additive White Gaussian Noise (AWGN) having the known variance, C_0 . Estimate the value of A from the measured signal, $x(t)$.

Solution: 2. Assuming Gauss-Markov theorem, after some straightforward derivations, the estimator is obtained as,

$$\hat{A}_{\text{MMSE}} = \frac{C_0}{T\sigma_A^2 + C_0} \bar{A} + \frac{\sigma_A^2}{T\sigma_A^2 + C_0} \int_0^T x(t) dt. \quad (15)$$

In addition, if $T\sigma_A^2 \gg C_0$, then the estimator can be simplified as,

$$\hat{A}_{\text{MMSE}} = \frac{C_0 \bar{A}}{T\sigma_A^2} + \frac{1}{T} \int_0^T x(t) dt. \quad (16)$$

■

Example 3. The samples received in a data packet of N symbols are expressed as, $x(i) = ps(i) + w(i)$, $i = 1, 2, \dots, N$, where p represents the channel attenuation, $s(i)$ is transmitted modulation symbol, and $w(i)$ is the sample of an AWGN. Discuss how to estimate the channel attenuation, p .

Solution: 3. The attenuation, p , is usually a complex-valued zero-mean Gaussian random variable. Since estimating unknown p while also detecting unknown $s(i)$ at the same time is not possible, the first n out of N data symbols are usually reserved for so-called pilot symbols, which are known at the receiver. For example, let $s(i) = s_0$, for $i = 1, \dots, n$. Then, the received symbols, ps_0 , have zero mean, and the variance, $E[|ps_0|^2] = E[|p|^2] |s_0|^2$, and Gauss-Markov theorem can be used to estimate, ps_0 , i.e., to estimate, p . ■

B. The MAP Estimator

If P is a discrete random variable, then it is meaningful to define its estimation error as,

$$\mu(\hat{P}, P) = \begin{cases} 0 & \hat{P} = P \\ 1 & \hat{P} \neq P. \end{cases} \quad (17)$$

The corresponding risk is equal to the probability of error, i.e.,

$$E[\mu(\hat{P}(X), P)] = \Pr(\hat{P}(X) \neq P) = 1 - \Pr(\hat{P}(X) = P). \quad (18)$$

This yields the MAP estimator,

$$\begin{aligned} \hat{P}_{\text{MAP}}(X) &= \underset{p_i}{\text{argmin}} E[\mu(p_i, P) | X = x] \\ &= \underset{p_i}{\text{argmax}} \Pr(P = p_i | X = x). \end{aligned} \quad (19)$$

If P is a continuous random variable, then the estimation error can be defined as,

$$\mu(\hat{P}, P) = \begin{cases} 0 & |\hat{P}(X) - P| < \Delta \\ 1 & |\hat{P}(X) - P| \geq \Delta. \end{cases} \quad (20)$$

If Δ in (20) is small, i.e., the probability that \hat{P} is close to P is large, then,

$$\begin{aligned} \hat{R}_{\text{MAP}}(X) &= \underset{\hat{P}}{\text{argmax}} f_{P|X}(\hat{P} | X = x) \\ &= \underset{\hat{P}}{\text{argmax}} f_{X|P}(x | \hat{P}) f_P(\hat{P}) \end{aligned} \quad (21)$$

where $f_{X|P}(x | \hat{P})$ represents the likelihood function. In practice, the maximum can be obtained by assuming the derivatives, i.e., $\frac{d}{d\hat{P}} f_{X|P}(x, \hat{P}) f_P(\hat{P}) = 0$, or, $\frac{d}{d\hat{P}} \log(f_{X|P}(x, \hat{P}) f_P(\hat{P})) = 0$.

III. GENERAL ESTIMATION OF NON-RANDOM PARAMETERS

The estimators introduced in the previous subsection require that the prior statistical description of the parameters to be estimated is completely known. If this is not the case, then the parameters can be treated as being non-random. The caveat is that the estimator of a non-random parameter, P , is often much more difficult to find, and it may not even exist. For example, assuming the MMSE criterion, minimizing the risk, $E[\mu(\hat{P}(X), P)] = \int_{\{X\}} (\hat{P}(X) - P)^2 f_X(x, P) dx$, yields correct, but otherwise useless solution, $\hat{P} = P$. Figure 6 shows the examples when the optimum estimator (in the sense of minimizing the average risk) exists, and when it does not exist.

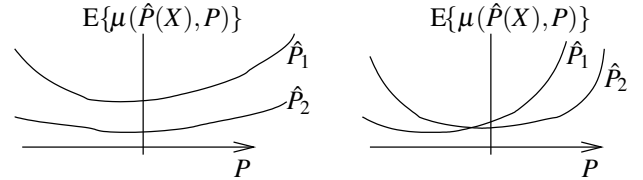


Figure 6. The examples when the optimum estimator exists (left), and when it does not exist (right).

The estimation of a non-random parameter, P , generally relies on knowledge of the statistical dependence of the measured values, X , i.e., on the parameterized PDF or PMF, $f_X(x, P)$, or, $\Pr_X(x, P)$, respectively, which must satisfy,

$$\int_{\{X\}} f_X(x, P) dx = 1, \quad \text{or,} \quad \sum_{x \in \{X\}} \Pr(X = x, P) = 1, \quad \forall P. \quad (22)$$

A. The MVUB Estimator

The minimum variance unbiased (MVUB) estimator of a non-random parameter, P , is unbiased, i.e., $E[\hat{P}] = P$, for $\forall P$. The variance of the estimation error of an unbiased estimator is,

$$\text{var}[\hat{P}(X) - P] = \underbrace{E[(\hat{P}(X) - P)^2]}_{\text{MSE}} = \text{var}[\hat{P}(X)]. \quad (23)$$

Consequently, the MVUB estimator minimizes the MSE equal to the variance of \hat{P} . However, the MVUB estimator may not exist, i.e., there may be no such function of X having the smallest variance for any value of P , as shown in Figure 6.

There are several important notions to describe the asymptotic accuracy of the estimators of non-random parameters. In particular, the CRLB defines the minimum achievable variance

of any unbiased estimator of a non-random parameter, P . It is mathematically formulated as,

$$\text{var}[\hat{P}] \geq \frac{1}{J(P)} \quad (24)$$

where Fisher information, $J(P)$, is computed as,

$$J(P) = \text{E} \left[\left(\frac{\partial \ln f_X(x, P)}{\partial P} \right)^2 \right] = \text{E} \left[-\frac{\partial^2 \ln f_X(x, P)}{\partial P^2} \right]. \quad (25)$$

Note that, $\ln f_X(x, P)$, represents the log-likelihood function, and showing the equality between the two expectations in (25) requires a derivation.

The estimator is said to be *efficient*, provided that it is unbiased, and it attains the CRLB defined in (24). Furthermore, the estimator is said to be *consistent*, provided that the variance, $\text{var}[\hat{P}]$, is decreasing with the number of measurements, X .

Remark 3. *There may be estimators that are slightly biased, but which have the variance smaller than the CRLB. For example, the estimator design can be constrained as, $\text{E}[|\hat{P} - P|] < \Delta$, to allow that it may possibly be unbiased. The trade-off between the bias and the variance frequently appears in training the machine learning models. Moreover, the consistency guarantees that collecting more data samples improves the estimator accuracy, which is also useful for machine learning.*

B. The ML Estimator

The MVUB estimator may not exist, or it is difficult to find. However, given the measurement, $X = x$, unless we are very unlucky, it is meaningful to choose the estimate of P to be the value with the largest likelihood, i.e.,

$$\begin{aligned} \hat{P}_{\text{ML}}(X) &= \text{argmax}_{\hat{P}} f_X(x, \hat{P}), \text{ or} \\ \hat{P}_{\text{ML}}(X) &= \text{argmax}_{\hat{P}} \Pr_X(X = x, \hat{P}). \end{aligned} \quad (26)$$

The estimator (26) is referred to as the ML estimator.

The ML estimator has the following properties.

- If the efficient estimate exists, then it is the ML estimate.
- If the efficient estimate does not exist, then the ML estimate is neither guaranteed to have the minimum variance, nor to be unbiased.
- The ML estimator is asymptotically unbiased as well as asymptotically efficient.
- The ML estimator is invariant to any function, $g(P)$, i.e., the ML estimate of $g(P)$ can be obtained as,

$$\hat{g}_{\text{ML}}(P) = g(\hat{P}_{\text{ML}}). \quad (27)$$

Remark 4. *Even though the ML estimator may not be unbiased, it is generally very attractive for its simplicity to obtain it. Moreover, if all the values of P are a priori equally likely, then the ML estimator and the MAP estimator are identical.*

Example 4. *There were x errors detected in a binary sequence of n bits. Assuming that the errors are independent, and they occur with the probability, P , decide whether the estimator $\hat{P} = x/n$ of P is the MVUB estimator.*

Solution: 4. The variance of the estimator, $\hat{P} = x/n$, is, $\text{var}[\hat{P}] = P(1 - P)/n$. The probability of x errors occurring among n bits is, $\Pr(X = x, P) = \binom{n}{x} P^x (1 - P)^{n-x}$, so that $\frac{\partial}{\partial P} \ln \Pr(X = x, P) = \frac{n}{P(1-P)} \left(\frac{x}{n} - P \right)$. Since the estimator, $\hat{P} = x/n$, can be shown to be unbiased, and $\text{E} \left[\left(\frac{\partial \ln \Pr(X=x, P)}{\partial P} \right)^2 \right] = \text{var}[\hat{P}]^{-1}$, the estimator is indeed the MVUB estimator. ■

Example 5. *The N samples of an unknown constant a were sampled in a zero-mean AWGN with an unknown variance, σ^2 . Find the ML estimate of a .*

Solution: 5. Assuming, $x(i) = a + w(i)e$, the joint PDF of N observed samples is,

$$f_X(x, a, \sigma) = \frac{1}{\sqrt{(2\pi\sigma)^N}} \exp \left(-\frac{1}{2\sigma^2} \sum_{i=1}^N (x(i) - a)^2 \right). \quad (28)$$

The ML estimates of the unknown parameters, a and σ , respectively, must satisfy,

$$\begin{aligned} \frac{\partial \ln f_X(x, \hat{a}_{\text{ML}}, \hat{\sigma}_{\text{ML}})}{\partial \hat{a}_{\text{ML}}} &= \frac{1}{\hat{\sigma}_{\text{ML}}} \sum_{i=1}^N (x(i) - \hat{a}_{\text{ML}}) \stackrel{!}{=} 0 \\ \frac{\partial \ln f_X(x, \hat{a}_{\text{ML}}, \hat{\sigma}_{\text{ML}})}{\partial \hat{\sigma}_{\text{ML}}} &= -\frac{N}{2} \frac{1}{\hat{\sigma}_{\text{ML}}} + \frac{1}{2\hat{\sigma}_{\text{ML}}^2} \sum_{i=1}^N (x(i) - \hat{a}_{\text{ML}})^2 \stackrel{!}{=} 0. \end{aligned} \quad (29)$$

Solving these two equations for \hat{a}_{ML} and $\hat{\sigma}_{\text{ML}}$, their estimators become,

$$\begin{aligned} \hat{a}_{\text{ML}} &= \frac{1}{N} \sum_{i=1}^N x(i), \text{ and} \\ \hat{\sigma}_{\text{ML}} &= \frac{1}{N} \sum_{i=1}^N (x(i) - \hat{a}_{\text{ML}})^2. \end{aligned} \quad (30)$$

The estimate, \hat{a}_{ML} , has the mean, $\text{E}[\hat{a}_{\text{ML}}] = \frac{1}{N} \sum_{i=1}^N \text{E}[x(i)] = \frac{1}{N} \sum_{i=1}^N a = a$, and the variance of estimation error, $\text{E}[(\hat{a}_{\text{ML}} - a)^2] = \frac{1}{N^2} \sum_{i=1}^N \text{var}[x(i)] = \frac{1}{N^2} \sum_{i=1}^N \sigma = \sigma/N$. On the other hand, for the estimate, $\hat{\sigma}_{\text{ML}}$, $\text{E}[\hat{\sigma}_{\text{ML}}] = \sigma \frac{N-1}{N}$, i.e., $\text{E}[\hat{\sigma}_{\text{ML}}] \neq \sigma$. Hence, the ML estimate of σ is only asymptotically unbiased, and the variance of estimation error, $\text{E}[(\hat{\sigma}_{\text{ML}} - \sigma)^2] = \sigma^2 \frac{2N-1}{N^2}$ becomes asymptotically (for large N) equal to the CRLB, $2\sigma^2/N$, proving that the ML estimator of σ is asymptotically efficient. ■

Many practical scenarios involve measurements in an AWGN. Specifically, in discrete time, assume the measured samples, $x(i) = g(p) + w(i)$, where $g(\cdot)$ denotes a non-linear function, and $w(i)$ is a zero-mean AWGN with unknown variance. The ML estimate of P is then,

$$\hat{P}_{\text{ML}} = \text{argmin}_{\hat{P}} \sum_{i=1}^N |x(i) - g(\hat{P})|^2. \quad (31)$$

Similarly, in continuous time, assume the observed signal, $x(t) = g(t, p) + w(t)$, over the time, $t \in (0, T)$, where $g(t, p)$ is a signal dependent on $P = p$, and $w(t)$ denotes a stationary zero-mean AWGN with unknown variance. The ML estimate of P is then,

$$\hat{P}_{\text{ML}} = \text{argmin}_{\hat{P}} \int_0^T |x(t) - g(t, \hat{P})|^2 dt. \quad (32)$$

Example 6. Find the ML estimate of a constant phase shift, θ , of the unmodulated carrier signal, $x(t) = A \cos(\omega_c t + \theta) + w(t)$, received over the time, $t \in (0, T)$, and assuming that, $\omega_c T \gg 1$.

Solution: 6. The ML estimate of θ is,

$$\begin{aligned} \hat{\theta}_{\text{ML}} &= \underset{\hat{\theta}}{\operatorname{argmin}} \int_0^T (x(t) - A \cos(\omega_c t + \hat{\theta}))^2 dt \\ &\approx \underset{\hat{\theta}}{\operatorname{argmax}} \int_0^T x(t) \cos(\omega_c t + \hat{\theta}) dt \\ &= \angle \underbrace{\int_0^T x(t) e^{-j\omega_c t} dt}_{X(\omega_c)}. \end{aligned} \quad (33)$$

Alternatively,

$$\begin{aligned} \frac{\partial}{\partial \hat{\theta}_{\text{ML}}} \ln f_X(x, A, \omega_c, \hat{\theta}_{\text{ML}}) &\stackrel{!}{=} 0 \\ \Rightarrow \int_0^T x(t) \sin(\omega_c t + \hat{\theta}_{\text{ML}}) dt &= 0. \end{aligned} \quad (34)$$

The corresponding implementations are shown in Figure 7. The bottom circuit in Figure 7 is a Phase-Locked Loop (PLL). It uses the output signal of a Voltage-Controlled Oscillator (VCO) to recover the carrier signal in order to enable the coherent detection of transmitted data symbols. ■

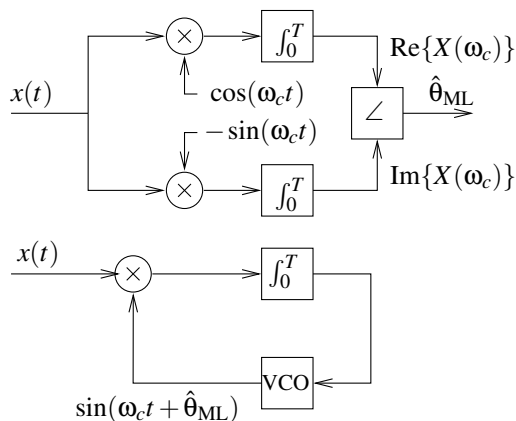


Figure 7. The two ML estimators of phase shift, θ , of the unmodulated noisy carrier signal, $x(t)$.

C. The LS Estimator

It may be sometimes impractical or impossible to obtain the distribution of the measurements, X . However, if a reasonably good model, $g(P)$, of $X(P)$ can be obtained, so that, $X(P) \approx g(P)$, then, the optimum estimator of the non-random parameter, P , can be defined as,

$$\hat{P}_{\text{opt}}(X) = \underset{\hat{P}}{\operatorname{argmin}} \mu(X, g(\hat{P})). \quad (35)$$

The corresponding LS estimator is obtained by assuming N measurements, X_i , and the error function,

$$\mu(X, g(\hat{P})) = \sum_{i=1}^N v_i (X_i - g(\hat{P}))^2 \quad (36)$$

where v_i are the weights to (de-)emphasize the measurements.

For time-continuous measurements, $x(t)$, the LS estimator is,

$$\hat{P}_{\text{LS}} = \underset{\hat{P}}{\operatorname{argmin}} \int_0^T (x(t) - g(t, \hat{P}))^2 dt. \quad (37)$$

If the parameter, P , is continuous, the minimization of (35) or (37) can be performed by differentiation, and then numerically find the root of a non-linear function.

Remark 5. The LS estimator corresponds to the ML estimator, provided that the measurement noise is AWGN.

D. The Moments Based Estimator

Both the ML and the LS estimators may be too complex to implement, since they require finding the extremum of a generally non-linear function. An alternative approach for estimating the non-random parameter is to match its statistical moments. In particular, the n -th general moment of a random variable, P , is defined as,

$$\begin{aligned} g_n(P) &= E_P[P^n] = \int_{\{P\}} p^n f_P(p) dp, \text{ or} \\ g_n(P) &= E_P[P^n] = \sum_{p \in \{P\}} p^n \Pr(P = p). \end{aligned} \quad (38)$$

If the measurements are stationary, i.e., they have the same moments, the n -th moment, $g_n(P)$, can be estimated from N measurements, x_i , as,

$$\hat{g}_n(P) = \frac{1}{N} \sum_{i=1}^N x_i^n. \quad (39)$$

Subsequently, the estimate of P is obtained by using the inverse function, g_n^{-1} , i.e.,

$$\hat{P} = g_n^{-1} \left(\frac{1}{N} \sum_{i=1}^N x_i^n \right). \quad (40)$$

Remark 6. In practice, the moments order, n , is typically assumed to be small, since it is more difficult to reliably estimate higher-order moments, and the estimation error increases with n . The estimator (40) is unbiased, and consistent, i.e., $\lim_{N \rightarrow \infty} \hat{g}_n(P) = g_n(P)$, however, there are otherwise no guarantees about its optimality. Note also that although the parameter, P , may be a random variable, its distribution is unknown, and thus, for the purpose of its estimation, it is considered to be non-random.

IV. LINEAR ESTIMATION OF RANDOM PARAMETERS

The general estimation strategy is to seek an optimum function to minimize the mean estimation error, i.e., the risk. This requires a full statistical description of measurements, X , as a function of the unknown parameter, P . Such a dependence is normally expressed as the conditional distribution, $f_{X|P}(x|p)$, or the conditional probability, $\Pr(X|P)$, when P is considered to be a random variable, and the parameterized distribution, $f_X(x; P)$, or the parameterized probability, $\Pr(X; P)$, when P is non-random.

Provided that only some statistics of the parameter, P , are known, such as its mean and the variance, they are sufficient

to define an optimum linear estimator. Such an estimator is simply a linear filter, which can be written as,

$$\hat{\mathbf{P}}(\mathbf{X}) = \mathbf{a} + \mathbf{H}\mathbf{X} \quad (41)$$

where \mathbf{X} is the vector of measurements, \mathbf{P} is the vector of parameters to be estimated, and $\hat{\mathbf{P}}(\mathbf{X})$ is the vector of the estimates. The vector \mathbf{a} and the matrix \mathbf{H} represent the filter coefficients, which are independent of the actual values, \mathbf{P} , and, \mathbf{X} . Consequently, given the statistics of \mathbf{X} and \mathbf{P} , such as, $E[\mathbf{X}]$, $\text{var}[\mathbf{X}]$, $E[\mathbf{P}]$, $\text{var}[\mathbf{P}]$, and $\text{cov}[\mathbf{P}, \mathbf{X}]$, the task is to find the optimum filter coefficients, \mathbf{a} , and, \mathbf{H} .

A. The LMMSE Estimator

The Linear MMSE (LMMSE) estimator is unbiased, i.e., $E[\hat{\mathbf{P}}(\mathbf{X})] = E[\mathbf{P}]$, or, $E[\hat{\mathbf{P}}(\mathbf{X}) - \mathbf{P}] = \mathbf{0}$, where $\mathbf{0}$ denotes the all-zeros vector. For the scalar, P , the LMMSE estimator minimizes the variance, $\text{var}[\hat{P}(X) - P] = E[(\hat{P}(X) - P)^2]$. In case of the vector, \mathbf{P} , the LMMSE estimator minimizes the correlation matrix,

$$\text{var}[\hat{\mathbf{P}}(\mathbf{X}) - \mathbf{P}] = E[(\hat{\mathbf{P}}(\mathbf{X}) - \mathbf{P})(\hat{\mathbf{P}}(\mathbf{X}) - \mathbf{P})^T]. \quad (42)$$

Remark 7. The square matrix, \mathbf{A} , is minimized, provided that it is positively semi-definite, i.e., $\mathbf{u}^T \mathbf{A} \mathbf{u} \geq 0$, as well as $\mathbf{u}^T \mathbf{A} \mathbf{u}$ has the minimum value for some non-zero vector, \mathbf{u} .

The LMMSE estimation minimizes the variance matrix, $\text{var}[\hat{\mathbf{P}}(\mathbf{X}) - \mathbf{P}]$. It is straightforward to show that the minimum occurs, when,

$$\mathbf{a} = \bar{\mathbf{P}} - \mathbf{H}\bar{\mathbf{X}}, \text{ and, } \mathbf{H} = \text{cov}[\mathbf{P}, \mathbf{X}] \text{var}^{-1}[\mathbf{X}] \quad (43)$$

requiring only knowledge of $\bar{\mathbf{P}} = E[\mathbf{P}]$, $\bar{\mathbf{X}} = E[\mathbf{X}]$, $\text{var}[\mathbf{X}]$, and $\text{cov}[\mathbf{P}, \mathbf{X}]$. The LMMSE estimate is then computed as,

$$\hat{\mathbf{P}}_{\text{LMMSE}}(\mathbf{X}) = \bar{\mathbf{P}} + \mathbf{H}(\mathbf{X} - \bar{\mathbf{X}}). \quad (44)$$

The LMMSE estimator has the following properties.

- The estimates are unbiased, i.e., $E[\hat{\mathbf{P}}_{\text{LMMSE}}(\mathbf{X})] = E[\mathbf{P}]$.
- The estimation error and the measurements are uncorrelated (orthogonal), i.e., $\text{cov}[\hat{\mathbf{P}}_{\text{LMMSE}} - \mathbf{P}, \mathbf{X}] = \mathbf{0}$.
- The estimation error and the estimate are uncorrelated, i.e., $\text{cov}[\hat{\mathbf{P}}_{\text{LMMSE}} - \mathbf{P}, \hat{\mathbf{P}}_{\text{LMMSE}}] = \mathbf{0}$.
- The variance matrix of the estimate, $\text{var}[\hat{\mathbf{P}}_{\text{LMMSE}}] = \mathbf{H} \text{var}[\mathbf{X}] \mathbf{H}^T = \mathbf{H} \text{cov}[\mathbf{X}, \mathbf{P}]$.
- The covariance matrix of the estimation errors is equal to,

$$\begin{aligned} \mathbf{S} &= E[(\hat{\mathbf{P}}_{\text{LMMSE}} - \mathbf{P})(\hat{\mathbf{P}}_{\text{LMMSE}} - \mathbf{P})^T] \\ &= \text{var}[\hat{\mathbf{P}}_{\text{LMMSE}} - \mathbf{P}] = \text{var}[\mathbf{P}] - \text{var}[\hat{\mathbf{P}}_{\text{LMMSE}}]. \end{aligned} \quad (45)$$

- The estimator, which is linear, unbiased and orthogonal, is the LMMSE estimator.

Example 7. The stationary signal, $x(t)$, with a known auto-covariance, $K_x(\tau) = E[(x(t+\tau) - \bar{x})(x(t) - \bar{x})]$, is sampled at three time instances, $t \in \{t_0 - \Delta t, t_0, t_0 + \Delta t\}$. Find the LMMSE estimate, $\hat{x}(t_0)$, of the derivative, $\frac{d}{dt}x(t)|_{t=t_0} = \dot{x}(t_0)$.

Solution: 7. Define the vectors, $P = \dot{x}(t_0)$, and, $\mathbf{X} = [x(t_0 - \Delta t), x(t_0), x(t_0 + \Delta t)]^T$. Then, the covariance functions are written as, $K_x(\tau) = K_x(-\tau)$, $K_{\dot{x},x}(\tau) = \dot{K}_x(\tau)$, $K_{x,\dot{x}}(\tau) = -\dot{K}_x(\tau)$, $K_{\dot{x}}(\tau) = -\dot{K}_x(\tau)$, and $\text{var}[\dot{x}(t_0)] = K_{\dot{x}}(0)$. The corresponding cross-covariance vector,

$$\text{cov}[P, \mathbf{X}] = [\dot{K}_x(\Delta t), \underbrace{\dot{K}_x(0)}_0, \underbrace{\dot{K}_x(-\Delta t)}_{-\dot{K}_x(\Delta t)}] \quad (46)$$

and the variance matrix,

$$\text{var}[\mathbf{X}] = \begin{bmatrix} K_x(0) & K_x(\Delta t) & K_x(2\Delta t) \\ K_x(\Delta t) & K_x(0) & K_x(\Delta t) \\ K_x(2\Delta t) & K_x(\Delta t) & K_x(0) \end{bmatrix}. \quad (47)$$

These expressions can be substituted into, $\hat{\mathbf{P}}_{\text{LMMSE}}(\mathbf{X}) = \bar{\mathbf{P}} + \mathbf{H}(\mathbf{X} - \bar{\mathbf{X}})$, and, $\mathbf{H} = \text{cov}[\mathbf{P}, \mathbf{X}] \text{var}^{-1}[\mathbf{X}]$, to get the estimator,

$$\begin{aligned} \hat{x}(t_0) &= \bar{x}(t_0) + \frac{\dot{K}_x(\Delta t)}{\underbrace{K_x(0) - K_x(2\Delta t)}_{\text{const}}} \times \\ &\quad (x(t_0 - \Delta t) - x(t_0 + \Delta t) - \bar{x}(t_0 - \Delta t) + \bar{x}(t_0 + \Delta t)). \end{aligned} \quad (48)$$

Example 8. The signal samples, $x(i)$, $i = 1, 2, \dots, n$, represent the sum of a random, but otherwise constant parameter, P , having the uniform probability distribution over the interval, $(0, d)$, and a stationary AWGN, $w(i)$, with zero-mean, and a known variance, σ_w^2 . The noise, $w(i)$, and the parameter, P , are independent. Find the LMMSE estimate of P .

Solution: 8. Define the vector, $\mathbf{X} = [x(1), \dots, x(n)]^T$, having the elements, $x(i) = P + w(i)$, so that, $\mathbf{X} = [1, \dots, 1]^T P + \mathbf{W}$. The parameter has the mean value, $E[P] = d/2$, and the variance, $\text{var}[P] = d^2/12$, while the noise, $E[w(i)] = 0$, and, $\text{var}[w(i)] = \sigma_w^2$. This yields the LMMSE estimator,

$$\hat{P}(n) = \frac{nd^2}{nd^2 + 12\sigma_w^2} \left(\frac{6\sigma_w^2}{nd} + \frac{1}{n} \sum_{i=1}^n x(i) \right). \quad (49)$$

V. LINEAR ESTIMATION OF NON-RANDOM PARAMETERS

If the vector of parameters, \mathbf{P} , is non-random, then, $E[\mathbf{P}] = \mathbf{P}$, and, $\text{cov}[\mathbf{P}, \mathbf{X}] = E[(\mathbf{P} - \mathbf{P})(\mathbf{X} - \bar{\mathbf{X}})^T] = \mathbf{0}$. Substituting these expressions into the LMMSE estimator, the solution, $\hat{\mathbf{P}}_{\text{LMMSE}} = \mathbf{P}$, is correct, but useless. As for general estimators of non-random parameters, a different strategy is required.

Assuming a class of linear unbiased estimators, i.e., the estimators of the form, $\hat{\mathbf{P}}(\mathbf{X}) = \mathbf{a} + \mathbf{H}\mathbf{X}$, then,

$$E[\hat{\mathbf{P}}(\mathbf{X})] = \mathbf{a} + \mathbf{H}\bar{\mathbf{X}} \stackrel{!}{=} \mathbf{P}, \quad \forall \mathbf{P} \quad (50)$$

and thus, $\bar{\mathbf{X}} = \mathbf{D}\mathbf{P} + \mathbf{r}$, such that, $\mathbf{H}\mathbf{D} = \mathbf{I}$, and, $\mathbf{a} = -\mathbf{H}\mathbf{r}$. The matrix, \mathbf{D} , and the vector, \mathbf{r} , are assumed to be known and independent of \mathbf{P} , where \mathbf{I} is the identity matrix. Consequently, the linear unbiased estimator of \mathbf{P} is written as,

$$\hat{\mathbf{P}} = \mathbf{H}(\mathbf{X} - \mathbf{r}) \quad (51)$$

under the constraints,

$$\bar{\mathbf{X}} = E[\mathbf{X}] = \mathbf{D}\mathbf{P} + \mathbf{r}, \text{ and, } \mathbf{H}\mathbf{D} = \mathbf{I}. \quad (52)$$

A. The BLUE Estimator

The Best Linear Unbiased Estimator (BLUE) is a linear estimation with the smallest variance. If the number of measurements (the length of vector, \mathbf{X}), is equal to the number of parameters to be estimated (the length of vector, \mathbf{P}), then the BLUE estimator is defined as,

$$\hat{\mathbf{P}} = \mathbf{H}(\mathbf{X} - \mathbf{r}), \quad \mathbf{H} = \mathbf{D}^{-1}. \quad (53)$$

On the other hand, if the length of vector, \mathbf{X} , is greater than the length of vector, \mathbf{P} , which is often the case, then the BLUE estimator is defined as the one that minimizes the correlation matrix of the estimation error, i.e.,

$$\begin{aligned} \mathbf{S} &= E[\underbrace{(\hat{\mathbf{P}}(\mathbf{X}) - \mathbf{P})(\hat{\mathbf{P}}(\mathbf{X}) - \mathbf{P})^T}_{\text{correlation matrix}}] = \underbrace{\text{var}[\hat{\mathbf{P}}(\mathbf{X}) - \mathbf{P}]}_{\text{variance matrix}} \\ &= \text{var}[\mathbf{H}(\mathbf{X} - \bar{\mathbf{X}})] = \mathbf{H}\text{var}[\mathbf{X}]\mathbf{H}^T. \end{aligned} \quad (54)$$

Thus, the matrix, \mathbf{S} , is equal to the variance matrix of the estimation error, since the estimator is unbiased, and it also equal to the variance matrix of the estimate, since \mathbf{P} is considered to be non-random.

Furthermore, if $\text{var}[\mathbf{X}]$ is independent of \mathbf{P} , which is not always guaranteed, the BLUE estimator, $\hat{\mathbf{P}} = \mathbf{H}(\mathbf{X} - \mathbf{r})$, is defined by the matrix,

$$\mathbf{H} = (\mathbf{D}^T \text{var}^{-1}[\mathbf{X}]\mathbf{D})^{-1} \mathbf{D}^T \text{var}^{-1}[\mathbf{X}]. \quad (55)$$

The corresponding correlation matrix is then,

$$\mathbf{S} = (\mathbf{D}^T \text{var}^{-1}[\mathbf{X}]\mathbf{D})^{-1}. \quad (56)$$

Example 9. The radar determines the distance to a target using three measurements, x_1 , x_2 and x_3 . The measurements are distorted by a zero-mean additive errors, w_i , $i = 1, 2, 3$. The correlations between the measurements are dependent on their separation in time, i.e., (a) if the time separation is T_1 , then, $r_{12} = r_{23} = 0.9$, and, $r_{13} = 0.7$; (b) if the time separation is T_2 , then $r_{12} = r_{23} = 0.7$, and, $r_{13} = 0.4$; and (c) if the time separation is T_3 , then $r_{12} = r_{23} = r_{13} = 0$. Obtain the BLUE estimator of the distance from the three measurements, and also calculate the mean square error of the estimate. Assume that the variance of the measurement errors is, $\text{var}[w_i] = 30 \text{ m}^2$.

Solution: 9. In this case, the vector, \mathbf{D} , and the variance matrix of \mathbf{X} are defined, respectively, as,

$$\mathbf{D} = \begin{bmatrix} 1 \\ 1 \\ 1 \end{bmatrix}, \quad \text{var}[\mathbf{X}] = 30 \begin{bmatrix} 1 & r_{12} & r_{13} \\ r_{12} & 1 & r_{23} \\ r_{13} & r_{23} & 1 \end{bmatrix}. \quad (57)$$

After substituting the specific values for the correlation coefficients, r_{12} , r_{23} , and r_{13} , the matrices, $\text{var}^{-1}[\mathbf{X}]$, and, the vector, $\mathbf{D}^T \text{var}^{-1}[\mathbf{X}]$, can be computed including the scalar value, $\mathbf{D}^T \text{var}^{-1}[\mathbf{X}]\mathbf{D}$. Subsequently, the estimators and their

mean square errors are obtained for each case of the time-separation, i.e.,

- (a) T_1 : $\hat{p} = x_1 - x_2 + x_3$, $S = 24 \text{ m}^2$;
- (b) T_2 : $\hat{p} = (x_1 + x_3)/2$, $S = 21 \text{ m}^2$;
- (c) T_3 : $\hat{p} = (x_1 + x_2 + x_3)/3$, $S = 10 \text{ m}^2$.

Remark 8. In Example 9, if the measurements are uncorrelated, the estimate is a simple arithmetic average, and the estimator variance is the smallest. In other two cases, the unequal combining weights account for the non-zero correlations between the measurements.

VI. ADDITIONAL SOLVED PROBLEMS

Example 10. An unmodulated carrier is measured in discrete time in the presence of a zero-mean AWGN with an unknown variance, σ_w^2 , i.e.,

$$x(i) = A \cos(\beta i + \Phi) + w(i), \quad i = 1, 2, \dots, N \quad (58)$$

where β is a known angular frequency, which can be assumed to be, $-\pi < \beta < \pi$, A is a Rayleigh distributed random amplitude, and Φ is a uniformly distributed random phase over the interval, $(-\pi, \pi)$. The amplitude, A , and the phase, Φ , are independent, and let the measured mean received power be also known. Find the MAP estimate of the phase Φ .

Solution: 10. The amplitude A is a nuisance parameter, which can be averaged out from the likelihood function, $f_{X|A, \Phi}(x|a, \phi)$, of the received signal, $x(i)$. Provided that,

$$\left| \frac{\sin(N\beta)}{N \sin(\beta)} \right| \ll 1, \quad (59)$$

the MAP estimate of Φ is obtained as (after some derivations),

$$\hat{\Phi}_{\text{MAP}} = -\angle(I + jQ) \quad (60)$$

where

$$\begin{aligned} I &= \sum_{i=1}^N x(i) \cos(\beta i) \\ Q &= \sum_{i=1}^N x(i) \sin(\beta i). \end{aligned} \quad (61)$$

Example 11. An unmodulated carrier with unknown amplitude, phase and angular frequency is measured in a zero-mean AWGN with an unknown variance, σ_w^2 , i.e.,

$$x(i) = A \cos(\beta i + \phi) + w(i), \quad i = 0, 1, \dots, N-1 \quad (62)$$

where $\beta \in (0, \pi)$. Find the ML estimate of all the unknown parameters, provided that $|\sin(N\beta)/(N \sin(\beta))| \ll 1$.

Solution: 11. The unknown parameters are: ϕ , A , β , and σ_w^2 . Define the quantities,

$$\begin{aligned} k^* &= \underset{k=0,1,\dots,N/2}{\text{argmax}} \left| \sum_{i=0}^{N-1} x(i) e^{-j\frac{2\pi}{N}ki} \right| \\ D_{k^*} &= \sum_{i=0}^{N-1} x(i) e^{-j\frac{2\pi}{N}k^*i}. \end{aligned} \quad (63)$$

The corresponding ML estimates are then computed as,

$$\begin{aligned} \hat{\beta}_{\text{ML}} &= \frac{2\pi}{N} k^*, & \hat{A}_{\text{ML}} &= \frac{2}{N} |D_{k^*}|, \\ \hat{\phi}_{\text{ML}} &= \angle D_{k^*}, & \hat{\sigma}_{w\text{ML}}^2 &= \frac{1}{N} \sum_{i=1}^N x^2(i) - \frac{2}{N^2} |D_{k^*}|^2. \end{aligned} \quad (64)$$

Example 12. As shown in Figure 8, the distance from an object at unknown locations, P_1 , and, P_2 , is measured at multiple spatial locations, $x_i = (i-1)\Delta$, $i = 1, 2, \dots, N$. Find the LS estimate of the object location.

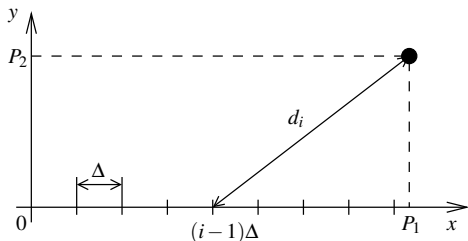


Figure 8. Determining the object location from multiple distance measurements.

Solution: 12. Denote the distances,

$$d_i = g_i(P_1, P_2) = \sqrt{(P_1 - x_i)^2 + P_2^2}. \quad (65)$$

The estimate, $[\hat{P}_1, \hat{P}_2]$, of the object location, $[P_1, P_2]$, is given by numerically solving the following set of non-linear equations:

$$\begin{aligned} \frac{1}{N} \sum_{i=1}^N \frac{d_i}{g_i(\hat{P}_1, \hat{P}_2)} &= 1 \\ \frac{2}{N(N-1)} \sum_{i=1}^N \frac{(i-1)d_i}{g_i(\hat{P}_1, \hat{P}_2)} &= 1. \end{aligned} \quad (66)$$

The initial location estimate can be computed as,

$$\begin{aligned} \hat{P}_1 &= \frac{d_1^2 - d_N^2 + (N-1)^2 \Delta^2}{2(N-1)\Delta} \\ \hat{P}_2 &= \pm \sqrt{d_1^2 - \hat{P}_1^2}. \end{aligned} \quad (67)$$

Example 13. A non-random discrete time signal, $p(i) = A \sin(\beta i + \phi)$, $i = 0, 1, 2, \dots$, is measured in a zero-mean AWGN with unknown variance, σ_w^2 . The frequency, β , is assumed to be known, whereas the amplitude, A , and the phase, ϕ , are unknown deterministic quantities. Find the LMMSE estimator (filter) to suppress the measurement noise at the current time instant, $i = n$. Then, simplify the estimator, provided that, $|\sin(n\beta)/\sin(\beta)| \ll 1$.

Solution: 13. The exact signal estimate and its variance, respectively, can be derived to be,

$$\begin{aligned} \hat{p}(n) &= \frac{1}{2g(n)\sin(\beta)} \times \\ &\sum_{i=0}^n x(i) (n \sin(\beta) \cos((n-i)\beta) - \sin(n\beta) \cos((i+1)\beta)) \\ S(n) &= \frac{\sigma_w^2}{2g(n)} \left(n + \frac{1}{2} - \frac{\sin((2n+1)\beta)}{2\sin(\beta)} \right) \end{aligned} \quad (68)$$

where

$$g(n) = \frac{1}{4} \left((n+1)^2 - \left(\frac{\sin(n\beta)}{\sin(\beta)} \right)^2 - \frac{\sin((2n+1)\beta)}{\sin(\beta)} \right). \quad (69)$$

If the condition, $|\sin(n\beta)/\sin(\beta)| \ll 1$, is valid, the estimator and its variance can be approximated as,

$$\begin{aligned} \hat{p}(n) &\approx \frac{2}{n+1} \sum_{i=0}^n x(i) \cos((n-i)\beta) \\ S(n) &\approx \frac{2}{n+1} \sigma_w^2. \end{aligned} \quad (70)$$

Example 14. A zero-mean discrete-time Gaussian random signal, $v(n)$, has the auto-covariance, $K_v(n) = \sigma_v^2 a^{|n|}$, $a > 0$. The signal, $v(n)$, is observed through a non-linear memoryless circuit having the output signal, $x(n) = \exp(kv(n))$, $k > 0$. Find the MMSE estimate, $\hat{x}(n)$, from the past samples, $x(i)$, $i = 1, 2, \dots, n-1$. Note that the random signal, $v(n)$, can be generated as,

$$v(n) = a v(n-1) + \sigma_v \sqrt{1-a^2} w(n) \quad (71)$$

where $v(1) = \sigma_v w(1)$, and $w(i)$ is the sample of a zero-mean, unit-variance AWGN.

Solution: 14. The extrapolated value, $x(n)$, is estimated as:

$$\hat{x}(n) = (x(n-1))^a \exp\left(\frac{1}{2} k^2 \sigma_v^2 (1-a^2)\right). \quad (72)$$

The variance of this estimator (predictor) can be found to be,

$$S = \exp(2k^2 \sigma_v^2) - \exp(k^2 \sigma_v^2 (1+a^2)). \quad (73)$$

VII. DISCUSSION

Estimation theory has been established decades ago. It is now the standard part of the undergraduate and graduate curricula in most engineering schools. It is then not surprising that many textbooks are available [1]–[17]. For example, good explanations of various topics in estimation theory at the intermediate level are provided in [7]. It should be noted that only textbooks are provided in the list of references. The survey of research papers and the state-of-the art are beyond the scope of this tutorial, which solely focuses on the fundamental principles of the parameter estimation.

Moreover, this tutorial could not cover many other important topics in parameter estimation. For instance, adaptive estimators estimate the values of multiple parameters successively rather than jointly in order to reduce the complexity. Bayesian inference relies on simple Bayes theorem; however, in practice, the underlying distributions cannot be obtained in closed-form, have many dimensions, or are only known up to a scaling constant. This requires to use sophisticated numerical algorithms involving sequential sampling, or approximations. Furthermore, estimating and predicting the values of time-dependent parameters is the subject of statistical filtering. It involves designing, e.g., Kalman filters and its variants, particle filters, and others. Importantly, signal estimation follows the same fundamental ideas of parameter estimation.

Computer simulations often perform implicit parameter estimations. It would be useful to consider the underlying parameter estimators explicitly as the components of simulations. This may be straightforward for point estimators, and it is more challenging for estimating, e.g., posterior distributions.

Unlike statistical inferences, the causal inferences are still a relatively new topic, which is not always included in the engineering curricula. Therefore, the textbooks on causal inferences are also a few and more recent [18]–[22]. A common strategy for performing causal inferences is to exploit the parameter inferences. In turn, the causal inference could enhance the parameter estimation methods.

Mathematical derivations rather than intuitive designs are often necessary to obtain the estimators, especially when the measurements are very noisy. Mathematical tractability for non-linear models can be achieved by assuming function linearization and other types of approximation. The estimator derivation translates the estimation problem into the corresponding optimization problem, and a procedure how to solve the optimization problem. This appears to be in a sharp contrast with nowadays nearly ubiquitous use of machine learning algorithms. These algorithms offer the solutions that are more flexible, but their design is based on intuition and extensive computer-based experimentation while avoiding complicated mathematical derivations altogether. Moreover, these algorithms can be implemented with a few lines of the Python code. The caveat is that the universal models used in supervised machine learning require large amounts of training data, they ignore excessive computational complexity, and their intuitive and experimental design often completely obscure their interpretability. This may explain why there are many computing libraries for machine learning, but only a few for parameter estimation.

Thus, having specialized, interpretable, but computationally efficient model-based estimators on one hand, and the universal, but inefficient model-free machine learning algorithms lacking the interpretability on the other hand indicates that there is a need to bring the principles of estimation theory into machine learning practice. For example, suppressing the measurement noise and adopting the model constraints by the means of estimation theory should greatly aid the machine learning to be either faster, or requiring less training data.

VIII. CONCLUSION

The choice of the appropriate estimator in a given signal processing scenario is completely dependent on what information is available. In particular, the model of measurements and of signals must be known, so that the statistical description of measurements and parameters to be estimated can be obtained in full, or at least partially. For instance, if the prior distribution of parameters is not known, these parameters are considered to be non-random, and their estimator may be much more difficult to find, or may not even exist. The lack of model knowledge can be replaced by the input-output samples as in the supervised machine learning. Another important consideration is how noisy the measurements are.

ACKNOWLEDGMENT

This tutorial is freely based on the undergraduate textbook [23] by Prof. Zdeněk Hrdina. E-mail: hrd@email.cz

REFERENCES

- [1] R. C. Aster, B. Borchers, and C. H. Thurber, *Parameter Estimation And Inverse Problems*, 3rd ed. Elsevier, Amsterdam, Netherlands, 2019.
- [2] M. Barkat, *Signal Detection and Estimation*, 2nd ed. Artech House, Norwood, MA, USA, 2005.
- [3] D. D. Boos and L. Stefanski, *Essential Statistical Inference: Theory and Methods*. Spring, New York, USA, 2013.
- [4] G. Casella and R. L. Berger, *Statistical Inference*, 2nd ed. Duxbury, Thomson Learning, Pacific Grove, CA, USA, 2002.
- [5] C. W. Helstrom, *Elements of Signal Detection and Estimation*. Prentice Hall, Inc, Englewood Cliffs, NJ, USA, 1995.
- [6] R. V. Hogg, E. A. Tanis, and D. L. Zimmerman, *Probability Statistical Inference*, 9th ed. Pearson, Upper Saddle River, NJ, USA, 2015.
- [7] S. M. Kay, *Fundamentals of Statistical Signal Processing: Estimation Theory*. Prentice Hall, Upper Saddle River, NJ, USA, 1993, vol. I.
- [8] B. L. et al., *Classification, Parameter Estimation and State Estimation, An Engineering Approach Using MATLAB*, 2nd ed. John Wiley & Sons, Ltd, Hoboken, NJ, USA, 2017.
- [9] H. Liero and S. Zwanzig, *Introduction to the Theory of Statistical Inference*. CRC Press, Boca Raton, FL, USA, 2012.
- [10] H. S. Migon, D. Gamerman, and F. Louzada, *Statistical Inference, An Integrated Approach*, 2nd ed. CRC Press, Boca Raton, FL, USA, 2015.
- [11] D. J. Olive, *Statistical Theory and Inference*. Springer Int. Publishing, Switzerland, 2014.
- [12] M. J. Panik, *Statistical Inference, A Short Course*. John Wiley & Sons, Inc., Hoboken, NJ, USA, 2012.
- [13] E. Pitman, *Some Basic Theory for Statistical Inference*. CRC Press, Boca Raton, FL, USA, 2018.
- [14] H. V. Poor, *An Introduction to Signal Detection and Estimation*, 2nd ed. Springer-Verlag, New York, USA, 1994.
- [15] C. A. Rohde, *Introductory Statistical Inference with the Likelihood Function*. Springer Int. Publishing, Switzerland, 2014.
- [16] G. G. Roussas, *An Introduction to Probability and Statistical Inference*, 2nd ed. Elsevier, Amsterdam, Netherlands, 2015.
- [17] J. Thijssen, *A Concise Introduction to Statistical Inference*. CRC Press, Boca Raton, FL, USA, 2014.
- [18] G. W. Imbens and D. B. Rubin, *Causal Inference for Statistics, Social, and Biomedical Sciences, An Introduction*. Cambridge University Press, NY, USA, 2015.
- [19] J. Pearl, *Causality, Models, Reasoning, and Inference*, 2nd ed. Cambridge University Press, New York, NY, USA, 2009.
- [20] J. Pearl, M. Glymour, and N. P. Jewell, *Causal Inference In Statistics, A Primer*. John Wiley & Sons, Ltd, Hoboken, NJ, USA, 2016.
- [21] J. Peters, D. Janzing, and B. Schölkopf, *Elements of Causal Inference, Foundations and Learning Algorithms*. The MIT Press, Cambridge, MA, USA, 2017.
- [22] P. R. Rosenbaum, *Observation and Experiment, An Introduction to Causal Inference*. Harvard Univ. Press, Cambridge, MA, USA, 2017.
- [23] Z. Hrdina, *Statistical Radio-Engineering*. Publishing Company of the Czech Technical University of Prague, 1996, in Czech.

Design of Third-Order Tensorial RLS Adaptive Filtering Algorithms

Ionuț-Dorinel Fîciu
 Telecommunications Department
 POLITEHNICA Bucharest
 Bucharest, Romania
 email: ionut.ficiu22@gmail.com

Camelia Elisei-Iliescu
 CNS
 ROMATSA
 Bucharest, Romania
 email: camelia.elisei@romatsa.ro

Laura-Maria Dogariu
 Telecommunications Department
 POLITEHNICA Bucharest
 Bucharest, Romania
 email: ldogariu@comm.pub.ro

Constantin Paleologu
 Telecommunications Department
 POLITEHNICA Bucharest
 Bucharest, Romania
 email: pale@comm.pub.ro

Cristian-Lucian Stanciu
 Telecommunications Department
 POLITEHNICA Bucharest
 Bucharest, Romania
 email: cristian@comm.pub.ro

Cristian Anghel
 Telecommunications Department
 POLITEHNICA Bucharest
 Bucharest, Romania
 email: canghel@comm.pub.ro

Abstract—A recently developed Recursive Least-Squares (RLS) adaptive filter based on a Third-Order Tensor (TOT) decomposition technique, namely RLS-TOT, has proved to be efficient in system identification problems that target the estimation of long length impulse responses. This solution fits very well in echo cancellation scenarios, where the associated impulse response of the echo path can reach hundreds or even thousands of coefficients. In this short paper, we further discuss several strategies for improving the performance of RLS-TOT, focusing on its main parameters that control the convergence features.

Index Terms—adaptive filter; recursive least-squares algorithm; echo cancellation; tensor decomposition; convergence parameters

I. INTRODUCTION

Adaptive filtering algorithms are frequently involved in many real-world system identification problems [1]. Among them, the Recursive Least-Squares (RLS) algorithm represents a very appealing choice due to its fast convergence rate, which can be achieved even for highly correlated input signals [2]. However, the price to pay is a high computational complexity.

In this framework, the overall difficulty increases when dealing with the identification of long length impulse responses, which raise significant challenges in terms of the complexity, convergence/tracking, and accuracy of the solution. Even the “fast” (i.e., less complex) versions of the RLS algorithm face performance limitations in such scenarios [3]. A well-known example is related to echo cancellation, where the echo paths are usually modeled as finite impulse response filters that can reach hundreds/thousands of coefficients [4].

Exploiting the characteristics of the systems to be identified represents a natural path to follow, in order to overcome the main challenges related to the estimation of long length impulse responses. In this context, several recent works have focused on decomposition-based techniques that involve the Nearest Kronecker Product (NKP) and low-rank approximations [5]–[8]. In this framework, the NKP-based approach in conjunction with a Third-Order Tensor (TOT) decomposition

has been addressed in [9] and [10]. The resulting RLS-TOT algorithm combines the coefficients of three adaptive filters of much shorter lengths, which leads to important advantages in terms of the main performance criteria.

In this short paper, we explore several upcoming developments related to the RLS-TOT adaptive filtering algorithm, aiming to improve the overall performance by tuning its convergence features. In this context, we target the development of improved versions of this algorithm, by using variable forgetting factors and variable regularization parameters.

In the following, Section II presents the RLS-TOT algorithm. Next, Section III is dedicated to the results and discussions. Finally, Section IV concludes this paper.

II. RLS-TOT ALGORITHM

Let us consider a single-input single-output scenario with real-valued signals. The main goal is to identify an unknown impulse response with L real-valued coefficients, which are grouped into the column vector \mathbf{h} . Thus, at the discrete-time index n , the reference signal results in

$$d(n) = \mathbf{h}^T \mathbf{x}(n) + w(n) = y(n) + w(n), \quad (1)$$

where the superscript T denotes the transpose operator, the column vector $\mathbf{x}(n)$ contains the most recent L samples of the zero-mean input signal $x(n)$, $y(n) = \mathbf{h}^T \mathbf{x}(n)$ is the output signal, and $w(n)$ is a zero-mean additive noise, which is uncorrelated with $x(n)$.

Also, let us consider that the length of \mathbf{h} can be expressed as $L = L_{11}L_{12}L_2$, with $L_{11} \geq L_{12}$ and $L_{11}L_{12} \gg L_2$. Thus, the impulse response can be equivalently decomposed as [9]

$$\mathbf{h} = \sum_{l=1}^{L_2} \sum_{p=1}^P \mathbf{h}_2^l \otimes \mathbf{h}_{12}^{lp} \otimes \mathbf{h}_{11}^{lp}, \quad (2)$$

where $P < L_{12}$ and the (shorter) component impulse responses \mathbf{h}_{11}^{lp} , \mathbf{h}_{12}^{lp} , and \mathbf{h}_2^l have the lengths L_{11} , L_{12} , and

L_2 , respectively, while \otimes denotes the Kronecker product. The particular subscript/superscript notation indicates different set of vectors related to the component impulse responses, as shown in Table I (which summarizes the specific data structures). The development from [9] that led to (2) is based on the low-rank approach [5]. This is a reasonable approach, since in practice most of the system impulse responses are low rank, especially in the context of room acoustics [7].

In this decomposition framework, the main focus is the identification of the component impulse responses from (2). Thus, the identification of the impulse response \mathbf{h} (with $L = L_{11}L_{12}L_2$ coefficients) is reformulated as a combination of three sets of coefficients, i.e., \mathbf{h}_2^l of length L_2 (with $l = 1, 2, \dots, L_2$), \mathbf{h}_{12}^{lp} of length L_{12} , and \mathbf{h}_{11}^{lp} of length L_{11} (with $l = 1, 2, \dots, L_2$ and $p = 1, 2, \dots, P$). Correspondingly, related to these three sets, we need to estimate L_2^2 , $PL_{12}L_2$, and $PL_{11}L_2$ coefficients, respectively. For the common decomposition setup that involves $L_{11}L_{12} \gg L_2$ and $P \ll L_{12}$ [9], this represents an important dimensionality reduction, especially for large values of L .

In this context, let us consider that $\hat{\mathbf{h}}(n)$ is an estimate of the impulse response \mathbf{h} at the discrete-time index n , so that the a priori error signal results in

$$e(n) = d(n) - \hat{\mathbf{h}}^T(n-1)\mathbf{x}(n). \quad (3)$$

On the other hand, using the impulse response decomposition from (2), we can also express its estimate as $\hat{\mathbf{h}}(n) = \sum_{l=1}^{L_2} \sum_{p=1}^P \hat{\mathbf{h}}_2^l(n) \otimes \hat{\mathbf{h}}_{12}^{lp}(n) \otimes \hat{\mathbf{h}}_{11}^{lp}(n)$, where $\hat{\mathbf{h}}_2^l(n)$, $\hat{\mathbf{h}}_{12}^{lp}(n)$, and $\hat{\mathbf{h}}_{11}^{lp}(n)$ are three shorter impulse responses of length L_{11} , L_{12} , and L_2 , respectively. Thus, in order to construct the cost functions of the RLS-TOT algorithm, we can rewrite $e(n)$ in three equivalent ways, with the purpose of “extracting” each individual component. As a result, following the development from [10], the equations that defined the RLS-TOT are:

$$\begin{aligned} \mathbf{k}_{12,11}(n) &= \frac{\mathbf{P}_{12,11}(n-1)\mathbf{x}_{12,11}(n)}{\lambda_2 + \mathbf{x}_{12,11}^T(n)\mathbf{P}_{12,11}(n-1)\mathbf{x}_{12,11}(n)}, \\ \mathbf{k}_{2,11}(n) &= \frac{\mathbf{P}_{2,11}(n-1)\mathbf{x}_{2,11}(n)}{\lambda_{12} + \mathbf{x}_{2,11}^T(n)\mathbf{P}_{2,11}(n-1)\mathbf{x}_{2,11}(n)}, \\ \mathbf{k}_{2,12}(n) &= \frac{\mathbf{P}_{2,12}(n-1)\mathbf{x}_{2,12}(n)}{\lambda_{11} + \mathbf{x}_{2,12}^T(n)\mathbf{P}_{2,12}(n-1)\mathbf{x}_{2,12}(n)}, \\ \mathbf{P}_{12,11}(n) &= \lambda_2^{-1} \left[\mathbf{I}_{L_2^2} - \mathbf{k}_{12,11}(n)\mathbf{x}_{12,11}^T(n) \right] \mathbf{P}_{12,11}(n-1), \\ \mathbf{P}_{2,11}(n) &= \lambda_{12}^{-1} \left[\mathbf{I}_{PL_{12}L_2} - \mathbf{k}_{2,11}(n)\mathbf{x}_{2,11}^T(n) \right] \mathbf{P}_{2,11}(n-1), \\ \mathbf{P}_{2,12}(n) &= \lambda_{11}^{-1} \left[\mathbf{I}_{PL_{11}L_2} - \mathbf{k}_{2,12}(n)\mathbf{x}_{2,12}^T(n) \right] \mathbf{P}_{2,12}(n-1), \\ \hat{\mathbf{h}}_2(n) &= \hat{\mathbf{h}}_2(n-1) + \mathbf{k}_{12,11}(n)e(n), \\ \hat{\mathbf{h}}_{12}(n) &= \hat{\mathbf{h}}_{12}(n-1) + \mathbf{k}_{2,11}(n)e(n), \\ \hat{\mathbf{h}}_{11}(n) &= \hat{\mathbf{h}}_{11}(n-1) + \mathbf{k}_{2,12}(n)e(n), \end{aligned}$$

where λ_2 , λ_{12} , and λ_{11} are the forgetting factors, which are positive constants smaller than or equal to one. The rest of notation is detailed in Table I, where \mathbf{I}_{L_\bullet} denotes the identity matrix of size $L_\bullet \times L_\bullet$, and $\mathbf{0}_{L_\bullet}$ generally denotes an all-zeros column vector of length L_\bullet . As shown in Table I, the three

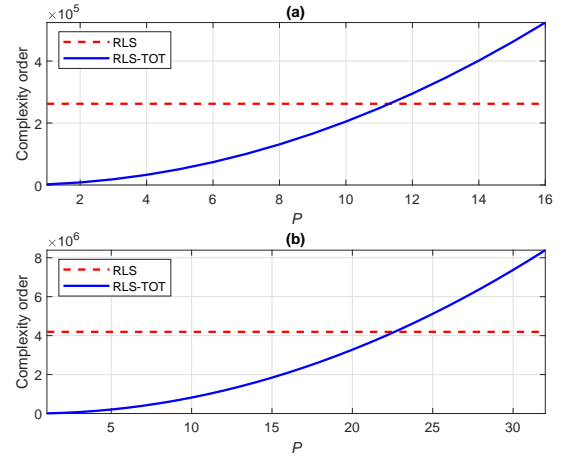


Figure 1. Complexity order of the conventional RLS algorithm and RLS-TOT for two impulse responses, with lengths (a) $L = 512$ and (b) $L = 2048$.

component impulse responses are connected via the Kronecker product, so that they are interdependent. The initialization setup is $\mathbf{P}_{12,11}(0) = \delta^{-1}\mathbf{I}_{L_2^2}$, $\mathbf{P}_{2,11}(0) = \delta^{-1}\mathbf{I}_{PL_{12}L_2}$, and $\mathbf{P}_{2,12}(0) = \delta^{-1}\mathbf{I}_{PL_{11}L_2}$, where $\delta > 0$ is the regularization parameter. Also, the components of the filters are initialized with $\hat{\mathbf{h}}_2^l(0) = [1 \ \mathbf{0}_{L_2-1}^T]^T$, $\hat{\mathbf{h}}_{12}^{lp}(0) = [1 \ \mathbf{0}_{L_{12}-1}^T]^T$, and $\hat{\mathbf{h}}_{11}^{lp}(0) = [1 \ \mathbf{0}_{L_{11}-1}^T]^T$.

The computational complexity of the RLS-based algorithms is proportional to the square of the filter length [2]. Thus, the conventional RLS algorithm requires a computational amount proportional to $\mathcal{O}(L^2) = \mathcal{O}(L_{11}L_{12}L_2)^2$. On the other hand, the RLS-TOT combines three much shorter filters (for the common setup of the decomposition parameters), so that it has a lower computational complexity order, i.e., $\mathcal{O}[L_2^4 + (PL_{11}L_2)^2 + (PL_{12}L_2)^2]$. This aspect is indicated in Figure 1, where the complexity orders of the conventional RLS algorithm and RLS-TOT are plotted, considering two impulse responses with $L = 512$ and $L = 2048$. For $L = 512$, the decomposition setup of the RLS-TOT involves $L_2 = 2$ and $L_{11} = L_{12} = 16$, while for $L = 2048$ we use $L_2 = 2$ and $L_{11} = L_{12} = 32$. Note that the value of P is usually significantly smaller than L_{12} , while $L_{12} \ll L$. Consequently, the computational complexity order of the RLS-TOT can be much lower as compared to the conventional RLS algorithm.

In the analysis reported in [10], the RLS-TOT was compared to the conventional RLS algorithm, but also with a previously developed decomposition-based version that exploits a second-order decomposition level, which is referred as the RLS algorithm using the NKP decomposition, i.e., RLS-NKP [6]. This counterpart combines the estimates provided by two adaptive filters of lengths $P^*L_1^*$ and $P^*L_2^*$, with $L = L_1^*L_2^*$ and $P^* < L_2^*$. While the RLS-TOT is able to outperform the conventional RLS benchmark and also the RLS-NKP, there is still room for improvements, as outlined in the next section.

TABLE I
 NOTATION USED FOR THE RLS-TOT ALGORITHM.

 Indices: $l = 1, 2, \dots, L_2$, $p = 1, 2, \dots, P$

Initialization:

$$\hat{\mathbf{h}}_2(0) = \begin{bmatrix} (\hat{\mathbf{h}}_2^{L_2})^T(0) & \dots & (\hat{\mathbf{h}}_2^1)^T(0) \end{bmatrix}^T$$

$$\hat{\mathbf{h}}_{12}^l(0) = \begin{bmatrix} (\hat{\mathbf{h}}_{12}^{l1})^T(0) & \dots & (\hat{\mathbf{h}}_{12}^{lP})^T(0) \end{bmatrix}^T$$

$$\hat{\mathbf{h}}_{12}(0) = \begin{bmatrix} (\hat{\mathbf{h}}_{12}^1)^T(0) & \dots & (\hat{\mathbf{h}}_{12}^{L_2})^T(0) \end{bmatrix}^T$$

$$\hat{\mathbf{h}}_{11}^l(0) = \begin{bmatrix} (\hat{\mathbf{h}}_{11}^{l1})^T(0) & \dots & (\hat{\mathbf{h}}_{11}^{lP})^T(0) \end{bmatrix}^T$$

$$\hat{\mathbf{h}}_{11}(0) = \begin{bmatrix} (\hat{\mathbf{h}}_{11}^1)^T(0) & \dots & (\hat{\mathbf{h}}_{11}^{L_2})^T(0) \end{bmatrix}^T$$

 For discrete-time index $n = 1, 2, \dots$

$$\hat{\mathbf{H}}_{12,11}^{lp}(n-1) = \mathbf{I}_{L_2} \otimes \hat{\mathbf{h}}_{12}^{lp}(n-1) \otimes \hat{\mathbf{h}}_{11}^{lp}(n-1)$$

$$\hat{\mathbf{H}}_{12,11}^l(n-1) = \sum_{p=1}^P \hat{\mathbf{H}}_{12,11}^{lp}(n-1)$$

$$\hat{\mathbf{H}}_{12,11}(n-1) = \begin{bmatrix} \hat{\mathbf{H}}_{12,11}^1(n-1) & \dots & \hat{\mathbf{H}}_{12,11}^{L_2}(n-1) \end{bmatrix}$$

$$\hat{\mathbf{H}}_{2,11}^{lp}(n-1) = \hat{\mathbf{h}}_2^l(n-1) \otimes \mathbf{I}_{L_{12}} \otimes \hat{\mathbf{h}}_{11}^{lp}(n-1)$$

$$\hat{\mathbf{H}}_{2,11}^l(n-1) = \begin{bmatrix} \hat{\mathbf{H}}_{2,11}^{l1}(n-1) & \dots & \hat{\mathbf{H}}_{2,11}^{lP}(n-1) \end{bmatrix}$$

$$\hat{\mathbf{H}}_{2,11}(n-1) = \begin{bmatrix} \hat{\mathbf{H}}_{2,11}^1(n-1) & \dots & \hat{\mathbf{H}}_{2,11}^{L_2}(n-1) \end{bmatrix}$$

$$\hat{\mathbf{H}}_{2,12}^{lp}(n-1) = \hat{\mathbf{h}}_2^l(n-1) \otimes \hat{\mathbf{h}}_{12}^{lp}(n-1) \otimes \mathbf{I}_{L_{11}}$$

$$\hat{\mathbf{H}}_{2,12}^l(n-1) = \begin{bmatrix} \hat{\mathbf{H}}_{2,12}^{l1}(n-1) & \dots & \hat{\mathbf{H}}_{2,12}^{lP}(n-1) \end{bmatrix}$$

$$\hat{\mathbf{H}}_{2,12}(n-1) = \begin{bmatrix} \hat{\mathbf{H}}_{2,12}^1(n-1) & \dots & \hat{\mathbf{H}}_{2,12}^{L_2}(n-1) \end{bmatrix}$$

$$\mathbf{x}_{12,11}(n) = \hat{\mathbf{H}}_{12,11}^T(n-1)\mathbf{x}(n)$$

$$\mathbf{x}_{2,11}(n) = \hat{\mathbf{H}}_{2,11}^T(n-1)\mathbf{x}(n)$$

$$\mathbf{x}_{2,12}(n) = \hat{\mathbf{H}}_{2,12}^T(n-1)\mathbf{x}(n)$$

$$\hat{\mathbf{h}}_2(n) = \begin{bmatrix} (\hat{\mathbf{h}}_2^{L_2})^T(n) & \dots & (\hat{\mathbf{h}}_2^1)^T(n) \end{bmatrix}^T$$

$$\hat{\mathbf{h}}_{12}(n) = \begin{bmatrix} (\hat{\mathbf{h}}_{12}^1)^T(n) & \dots & (\hat{\mathbf{h}}_{12}^{L_2})^T(n) \end{bmatrix}^T$$

$$\hat{\mathbf{h}}_{12}^l(n) = \begin{bmatrix} (\hat{\mathbf{h}}_{12}^{l1})^T(n) & \dots & (\hat{\mathbf{h}}_{12}^{lP})^T(n) \end{bmatrix}^T$$

$$\hat{\mathbf{h}}_{11}(n) = \begin{bmatrix} (\hat{\mathbf{h}}_{11}^1)^T(n) & \dots & (\hat{\mathbf{h}}_{11}^{L_2})^T(n) \end{bmatrix}^T$$

$$\hat{\mathbf{h}}_{11}^l(n) = \begin{bmatrix} (\hat{\mathbf{h}}_{11}^{l1})^T(n) & \dots & (\hat{\mathbf{h}}_{11}^{lP})^T(n) \end{bmatrix}^T$$

$$\hat{\mathbf{h}}(n) = \sum_{l=1}^{L_2} \sum_{p=1}^P \hat{\mathbf{h}}_2^l(n) \otimes \hat{\mathbf{h}}_{12}^{lp}(n) \otimes \hat{\mathbf{h}}_{11}^{lp}(n)$$

III. RESULTS AND DISCUSSIONS

The main parameters of the RLS-based algorithms are the forgetting factors. While the conventional RLS algorithm involves a single forgetting factor (denoted by λ), the RLS-

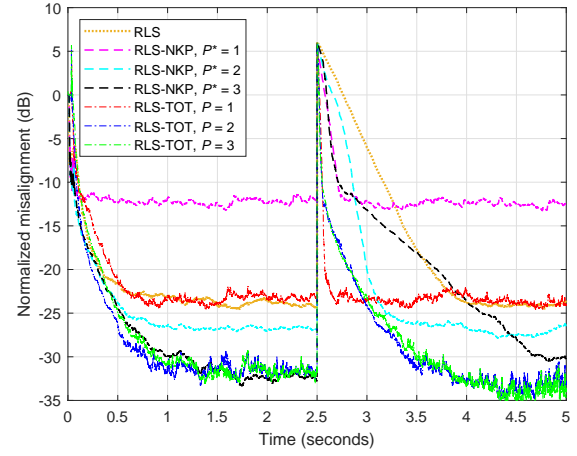


Figure 2. Misalignment of the RLS-based algorithms for the identification of a network impulse response of length $L = 512$. The forgetting factors are set based on (4), using $K = 5$ for the conventional RLS algorithm, and $K = 45$ for the RLS-NKP and RLS-TOT. The input signal is an AR(1) process and SNR = 20 dB.

TOT algorithm requires three forgetting factors, i.e., λ_{11} , λ_{12} , and λ_2 . Also, the RLS-NKP algorithm [6] uses two forgetting factors, λ_1^* and λ_2^* , which correspond to the two adaptive filters. It is known that choosing the value of a forgetting factor involves a compromise between the main performance criteria, i.e., fast convergence/tracking and low misalignment. In general, the value of a forgetting factor λ_* can be related to the associated filter length (generally denoted by L_*), according to the relation [6]:

$$\lambda_* = 1 - \frac{1}{KL_*}, \quad (4)$$

with $K \geq 1$. A higher value of K leads to λ_* closer to one, which improves the accuracy of the solution, but sacrificing in terms of the tracking behavior. We should also outline that the initial convergence rate is not always relevant for the RLS-based algorithms, while the tracking is the true assessment [3].

As compared to the conventional RLS algorithm, the RLS-TOT provides a better flexibility related to the choice of these parameters, since it combines three adaptive filters of different lengths, but much shorter as compared to the length of the global filter. Since a shorter adaptive filter is usually related to a faster tracking capability, we could increase the values of RLS-TOT forgetting factors, aiming to improve its accuracy, while slightly sacrificing in terms of tracking. On the other hand, the forgetting factors of the conventional RLS algorithm and the RLS-NKP should be increased in order to improve their tracking behavior, while paying in terms of accuracy.

Such an approach is considered in Figure 2, where the forgetting factors of the comparing algorithms are set based on (4), using $K = 5$ for the conventional RLS algorithm and $K = 45$ for the decomposition-based versions, i.e., RLS-NKP and RLS-TOT. The experimental framework is echo cancellation, aiming to identify a network echo path from G168 Recommendation [11], with the length $L = 512$ (the

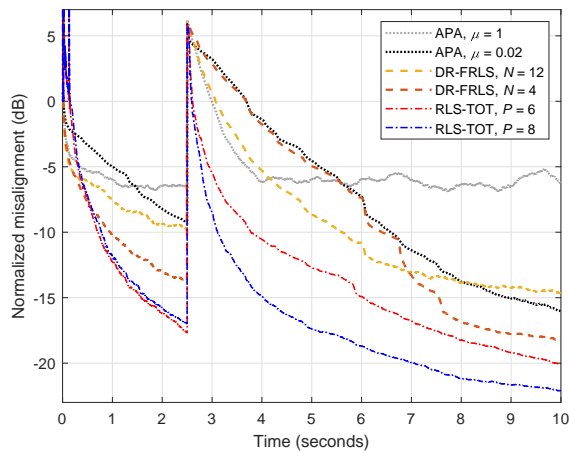


Figure 3. Misalignment of the APA, DR-FRLS algorithm, and RLS-TOT, for the identification of an acoustic impulse response of length $L = 2048$. The RLS-TOT uses λ_{11} and λ_{12} set based on (4), with $K = 100$, while $\lambda_2 = 1$. The input signal is speech and $\text{SNR} = 10$ dB.

sampling rate is 8 kHz). Thus, the decomposition setup uses $L_1^* = 32$ and $L_2^* = 16$ for the RLS-NKP, and $L_{11} = L_{12} = 16$ and $L_2 = 2$ for the RLS-TOT. The input signal $x(n)$ is a first order autoregressive process, AR(1), which is obtained by filtering a white Gaussian noise through an AR(1) transfer function with the pole at 0.8. The output of the echo path, $y(n)$, is corrupted by a white Gaussian noise, $w(n)$, while the signal-to-noise ratio (SNR) is set to 20 dB. In order to test the tracking capabilities, an abrupt change of the impulse response is considered, by changing the sign of the coefficients after 2.5 seconds. The performance measure is the normalized misalignment (in dB), which is evaluated as $20 \log_{10} \left[\frac{\|\mathbf{h} - \hat{\mathbf{h}}(n)\|}{\|\mathbf{h}\|} \right]$, where $\|\cdot\|$ denotes the Euclidean norm. As we can notice in Figure 2, the performance gain (i.e., misalignment/tracking) is clear in the favor of RLS-TOT, as compared to the RLS-NKP counterpart, for $P^* = P$. Besides, even if the tracking capability of the conventional RLS algorithm is improved when using a smaller value of K , it is significantly slower as compared to the RLS-TOT.

Another strategy that should be considered in case of the RLS-TOT is to set the maximum value of the forgetting factor (i.e., equal to 1) for the shortest filter of length L_2^* . In the common setups, this filter has only a few coefficients (e.g., 4 in our scenario), so that the tracking behavior of the global filter will be slightly affected, while still improving its misalignment. This is supported in Figure 3, in the framework of acoustic echo cancellation. This second experiment is dedicated to the identification of an acoustic impulse response of length $L = 2048$, using a speech signal as input and operating in a noisy environment with $\text{SNR} = 10$ dB. Therefore, the decomposition setup of the RLS-NKP considers $L_1^* = 64$ and $L_2^* = 32$, while the RLS-TOT uses $L_{11} = L_{12} = 32$ and $L_2 = 2$. Due to its high computational complexity, the conventional RLS algorithm is prohibitive in such scenarios

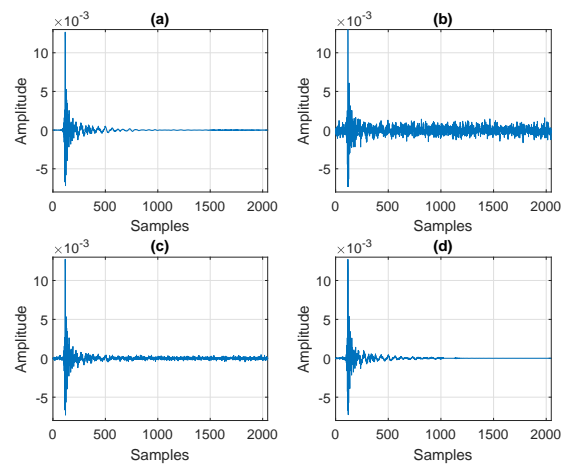


Figure 4. Impulse responses related to the experiment reported in Figure 3: (a) true acoustic impulse response \mathbf{h} ; (b) $\hat{\mathbf{h}}(n)$ obtained by APA using $\mu = 1$; (c) $\hat{\mathbf{h}}(n)$ obtained by DR-FRLS using $N = 12$; and (d) $\hat{\mathbf{h}}(n)$ obtained by RLS-TOT using $P = 8$.

that involve very long length impulse responses. Hence, other more practical algorithms are used in this simulation. First, we involve the Affine Projection Algorithm (APA) [12], which is a very popular choice in the framework of acoustic echo cancellation. The main parameters of APA are the step-size ($0 < \mu \leq 1$) and the projection order ($1 \leq M \ll L$). Higher values of μ and M improve the convergence rate and tracking of the algorithm, but increase the misalignment. In our scenario, we set $M = 8$ and use different values of μ to illustrate this behavior. Second, we involve in the experiment the recently developed Data-Reuse Fast RLS (DR-FRLS) algorithm [13]. This algorithm can operate with the maximum value of the forgetting factor (i.e., $\lambda = 1$), while the tracking capability is tuned based on the data-reuse parameter, denoted by N . As we can notice in Figure 3, the RLS-TOT outperforms both APA and the DR-FRLS algorithm, in terms of convergence rate/tracking and misalignment level.

The most relevant estimated impulse responses related to the experiment reported in Figure 3 are included in Figure 4. These are compared to the true acoustic impulse response \mathbf{h} of length $L = 2048$ [shown in Figure 4(a)]. Here, we compare the estimates provided by three algorithms: i) APA using $\mu = 1$ [Figure 4(b)], ii) DR-FRLS using $N = 12$ [Figure 4(c)], and iii) RLS-TOT using $P = 8$ [in Figure 4(d)]. As we can notice, the accuracy of the estimated impulse response of RLS-TOT is significantly better as compared to the estimates obtained by the comparing algorithms.

In future works, it would be interesting to investigate time-dependent (i.e., variable) forgetting factors. In this manner, by varying these parameters within the iterations of the main algorithm, we can target a better compromise between the performance criteria. In echo cancellation, this translates in addressing several challenging situations, like the echo path change, the double-talk scenario (i.e., the two speakers talk simultaneously), and the background noise variation.

In terms of double-talk robustness, an appealing approach would be to design variable regularization parameters for the RLS-TOT. To this purpose, the main relations of the algorithm (presented in Section II) need to be reformulated, by considering the covariance matrices

$$\mathbf{R}_{12,11}(n) = \sum_{k=1}^n \lambda_2^{n-k} \mathbf{x}_{12,11}(k) \mathbf{x}_{12,11}^T(k), \quad (5)$$

$$\mathbf{R}_{2,11}(n) = \sum_{k=1}^n \lambda_{12}^{n-k} \mathbf{x}_{2,11}(k) \mathbf{x}_{2,11}^T(k), \quad (6)$$

$$\mathbf{R}_{2,12}(n) = \sum_{k=1}^n \lambda_{11}^{n-k} \mathbf{x}_{2,12}(k) \mathbf{x}_{2,12}^T(k). \quad (7)$$

Their inverses are equivalent to the matrices $\mathbf{P}_{12,11}(n)$, $\mathbf{P}_{2,11}(n)$, and $\mathbf{P}_{2,12}(n)$. They can be iteratively evaluated as

$$\mathbf{R}_{12,11}(n) = \lambda_2 \mathbf{R}_{12,11}(n-1) + \mathbf{x}_{12,11}(n) \mathbf{x}_{12,11}^T(n), \quad (8)$$

$$\mathbf{R}_{2,11}(n) = \lambda_{12} \mathbf{R}_{2,11}(n-1) + \mathbf{x}_{2,11}(n) \mathbf{x}_{2,11}^T(n), \quad (9)$$

$$\mathbf{R}_{2,12}(n) = \lambda_{11} \mathbf{R}_{2,12}(n-1) + \mathbf{x}_{2,12}(n) \mathbf{x}_{2,12}^T(n), \quad (10)$$

so that the final updates of the filters result in

$$\hat{\mathbf{h}}_2(n) = \hat{\mathbf{h}}_2(n-1) + \mathbf{M}_{12,11}^{-1}(n) \mathbf{x}_{12,11}(n) e(n), \quad (11)$$

$$\hat{\mathbf{h}}_{12}(n) = \hat{\mathbf{h}}_{12}(n-1) + \mathbf{M}_{2,11}^{-1}(n) \mathbf{x}_{2,11}(n) e(n), \quad (12)$$

$$\hat{\mathbf{h}}_{11}(n) = \hat{\mathbf{h}}_{11}(n-1) + \mathbf{M}_{2,12}^{-1}(n) \mathbf{x}_{2,12}(n) e(n), \quad (13)$$

where $\mathbf{M}_{12,11}(n) = \mathbf{R}_{12,11}(n) + \delta_2 \mathbf{I}_{L_2^2}$, $\mathbf{M}_{2,11}(n) = \mathbf{R}_{2,11}(n) + \delta_{12} \mathbf{I}_{PL_{12}L_2}$, and $\mathbf{M}_{2,12}(n) = \mathbf{R}_{2,12}(n) + \delta_{11} \mathbf{I}_{PL_{11}L_2}$. The regularization parameters δ_2 , δ_{12} , and δ_{11} can be designed in a time-dependent manner, as a function of the estimated SNR. In other words, a lower SNR should be associated to higher values of the regularization terms, which further slow down the adaptation process. This is the desired behavior in double-talk situations or noisy environments, where a low SNR level could significantly disturb the echo canceler.

IV. CONCLUSIONS

In this short paper, we have presented a tensorial RLS-based algorithm, which follows a recently developed method that splits the impulse response of the system based on a third-order tensor decomposition. The resulting RLS-TOT combines the estimates provided by three shorter adaptive filters, so that it is suitable for the identification of long length impulse responses. We further investigated different strategies for this algorithm, focusing on its main parameters, i.e., the forgetting factors and the regularization terms. Simulations performed in echo cancellation scenarios support the performance gain, in terms of converge/tracking and accuracy of the solution.

ACKNOWLEDGMENTS

This work was supported by a grant of the Ministry of Research, Innovation and Digitization, CNCS-UEFISCDI, project number PN-III-P4-PCE-2021-0438, within PNCDI III. Dr. Camelia Elisei-Iliescu would like to acknowledge the support of ROMATSA. The authors would like to thank the three reviewers for the valuable comments and suggestions, which significantly improved the content of this paper.

REFERENCES

- [1] J. Benesty and Y. Huang, Eds., *Adaptive Signal Processing—Applications to Real-World Problems*. Berlin, Germany: Springer-Verlag, 2003.
- [2] S. Haykin, *Adaptive Filter Theory*. Fourth Edition, Upper Saddle River, NJ, USA: Prentice-Hall, 2002.
- [3] Y. V. Zakharov and V. H. Nascimento, “DCD-RLS adaptive filters with penalties for sparse identification,” *IEEE Trans. Signal Processing*, vol. 61, pp. 3198–3213, June 2013.
- [4] S. L. Gay and J. Benesty, Eds., *Acoustic Signal Processing for Telecommunication*. Boston, MA: Kluwer Academic Publisher, 2000.
- [5] C. Paleologu, J. Benesty, and S. Ciochină, “Linear system identification based on a Kronecker product decomposition,” *IEEE/ACM Trans. Audio, Speech, Language Processing*, vol. 26, pp. 1793–1808, Oct. 2018.
- [6] C. Elisei-Iliescu et al., “Recursive least-squares algorithms for the identification of low-rank systems,” *IEEE/ACM Trans. Audio, Speech, Language Processing*, vol. 27, pp. 903–918, May 2019.
- [7] L.-M. Dogariu, J. Benesty, C. Paleologu, and S. Ciochină, “Identification of room acoustic impulse responses via Kronecker product decompositions,” *IEEE/ACM Trans. Audio, Speech, Language Processing*, vol. 30, pp. 2828–2841, Sept. 2022.
- [8] H. He, J. Chen, J. Benesty, and Y. Yu, “A frequency-domain recursive least-squares adaptive filtering algorithm based on a Kronecker product decomposition,” in *Proc. IEEE ICASSP*, 2023, 5 pages.
- [9] J. Benesty, C. Paleologu, and S. Ciochină, “Linear system identification based on a third-order tensor decomposition,” *IEEE Signal Processing Lett.*, vol. 30, pp. 503–507, May 2023.
- [10] C. Paleologu et al., “Recursive least-squares algorithm based on a third-order tensor decomposition for low-rank system identification,” *Signal Processing*, vol. 213, id. 109216, Dec. 2023.
- [11] *Digital Network Echo Cancellers*, ITU-T Recommendation G.168, 2012.
- [12] K. Ozeki and T. Umeda, “An adaptive filtering algorithm using an orthogonal projection to an affine subspace and its properties,” *Electron. Commun. Jpn.*, vol. 67-A, pp. 19–27, May 1984.
- [13] C. Paleologu, J. Benesty, and S. Ciochină, “Data-reuse recursive least-squares algorithms,” *IEEE Signal Processing Lett.*, vol. 29, pp. 752–756, Mar. 2022.